Blue-shifted ancyromonad channelrhodopsins for multiplex optogenetics

Elena G. Govorunova[1], Oleg A. Sineshchekov[1], Hai Li[1], Yueyang Gou[2,3], Hongmei Chen[2,3], Shuyuan Yang[2], Yumei Wang[1], Stephen Mitchell[4], Alyssa Palmateer[4], Leonid S. Brown[4], François St-Pierre[2,5,6,7], Mingshan Xue[2,3,8], and John L. Spudich[1,9*]

[1]Center for Membrane Biology, Department of Biochemistry & Molecular Biology, The University of Texas Health Science Center at Houston McGovern Medical School, Houston, TX 77030, USA

[2]Department of Neuroscience, Baylor College of Medicine; Houston, TX 77030, USA

[3]The Cain Foundation Laboratories, Jan and Dan Duncan Neurological Research Institute at Texas Children's Hospital; Houston, TX 77030, USA

[4]Department of Physics and Biophysics Interdepartmental Group, University of Guelph; Guelph, Ontario N1G 2W1, Canada

[5]Department of Biochemistry and Molecular Biology, Baylor College of Medicine, Houston, TX 77030, USA

[6]Systems, Synthetic, and Physical Biology Program, Rice University, Houston, TX 77005, USA

[7]Department of Electrical and Computer Engineering, Rice University, Houston, TX 7705, USA

[8]Department of Molecular and Human Genetics, Baylor College of Medicine, Houston, TX 77030, USA

[*]Correspondence: john.l.spudich@uth.tmc.edu (J.L.S.)

Abstract

Light-gated ion channels from protists (channelrhodopsins or ChRs) are optogenetic tools widely used for controlling neurons and cardiomyocytes. Multiplex optogenetic applications require spectrally separated molecules that must be found in nature, as they are difficult to engineer without disrupting channel function. Scanning numerous sequence databases, we identified three robust naturally blue-shifted ChRs from ancyromonads. They form a separate branch on the phylogenetic tree and contain residue motifs characteristic of anion ChRs (ACRs). However, only two conduct chloride, whereas the close *Nutomonas longa* homolog (peak absorption at ~440 nm) generates inward cation currents in mammalian cells under physiological conditions, significantly exceeding those by previously known tools. Measurements of transient absorption changes and pH titration of purified *Ancyromonas sigmoides* ACR (*Ans*ACR) combined with mutant analysis revealed the roles of the residues in the photoactive site. Both ancyromonad ACRs allowed optogenetic silencing of mouse cortical neurons in brain slices. *Ans*ACR expression in the cholinergic neurons enabled photoinhibition of pharyngeal muscle contraction in live worms. *Ans*ACR could be activated by near-infrared two-photon illumination, which is required to control specific neurons in thick tissue. Our results improved the mechanistic understanding of light-gated channel function and expanded the optogenetic toolkit.

Impact statement: Ancyromonad channelrhodopsins advance our understanding of ionic selectivity and wavelength regulation in light-gated ion channels and also expand the toolkit for all-optical electrophysiology.

Introduction

Channelrhodopsins (ChRs) are retinylidene proteins acting as photoreceptors that mediate photomotility in green flagellate algae (Sineshchekov, Jung, & Spudich, 2002) and are found in other protist lineages. The chromophore is attached via a retinylidene Schiff base (RSB) linkage to a conserved lysine residue in the 7th transmembrane helix (TM7). Upon photoexcitation, ChRs generate passive ionic currents across the cell membrane and are used for optical control of excitable mammalian cells (optogenetics) (Deisseroth, 2021; Piatkevich & Boyden, 2023). The seven-transmembrane (7TM) domain is sufficient for channel activity; the role of the C-terminal domain comprising half of the polypeptide chain remains unclear. A considerable diversity within the ChR family suggests a convergent evolution of light-gated channel function (Govorunova, Sineshchekov, & Spudich, 2022). ChRs form dimers (Li et al., 2019; Volkov et al., 2017) or trimers (Morizumi et al., 2023; Tucker, Sridharan, Adesnik, & Brohawn, 2022), but their ionic conductance is intrinsic to individual protomers, unlike voltage- or ligand-gated channels, in which several protomers contribute to the channel pore. Anion channelrhodopsins (ACRs) generate photoinduced anion influx in mammalian cells; cation channelrhodopsins (CCRs) generate H^+ and Na^+ influx; and kalium channelrhodopsins (KCRs) generate K^+ efflux (Govorunova, Sineshchekov, & Spudich, 2022; Govorunova, Sineshchekov, & Spudich, 2023). ACRs and KCRs are used for optogenetic neuronal inhibition, and CCRs are used for neuronal activation.

Increasingly popular all-optical electrophysiology, i.e., simultaneous perturbation and measurement of membrane potential using light-sensitive actuators and reporters, respectively in the same genetically defined cells (Hochbaum et al., 2014) requires spectrally non-overlapping optogenetic tools. Even the most red-shifted ChRs retain sufficient sensitivity to blue light due to their relatively wide spectral bandwidth (Govorunova et al., 2020; Oda et al., 2018). The development of red-light-absorbing genetically encoded fluorescent biosensors for monitoring neural activity (Sakamoto & Yokoyama, 2024) opened up the possibility of pairing them with blue-shifted ChRs. Molecular engineering yielded several blue-shifted ChR versions (Kato et al., 2015), but mutagenetic perturbations of the binding pocket frequently harm channel function. A complementary approach is exploring natural ChR diversity to search for molecules with desired biophysical properties optimized by evolution. Approximately ~1,000 ChR sequences are currently known, but a much smaller number has been functionally characterized (Govorunova, Sineshchekov, & Spudich, 2022).

Here, we identified and characterized three ChR variants from bacterivorous ancyromonad flagellates. Ancyromonads (also known as planomonads) that represent a distinct major clade near the most commonly inferred root of the eukaryote tree (Brown et al., 2018). We conducted automated and manual patch clamp analysis of photocurrents upon expression of ancyromonad ChR cDNAs in cultured mammalian cells and transient absorption changes in detergent-purified proteins. We show that two ancyromonad ChRs are anion-selective, but the third, the most blue-shifted, conducts metal cations. We expressed ancyromonad ACRs in mouse cortical pyramidal neurons and demonstrated photoinhibition of action potentials in acute brain slices. The nematode *Caenorhabditis elegans* is an attractive model for analyzing nervous system function by optogenetic manipulation (Bergs, Henss, Glock, Nagpal, & Gottschalk, 2022). C. *elegans* feeds on bacteria by rhythmic contractions and relaxations (pumping) of its pharynx. The cholinergic pharyngeal neurons, primarily the MC neurons, entrain the pharyngeal muscle rhythm (Trojanowski, Raizen, & Fang-Yen, 2016). Neuronal and muscular electrical activity leading to pharyngeal contractions can be monitored non-invasively by electropharyngeogram (EPG) recording

(Raizen & Avery, 1994). We used this approach to demonstrate that a blue-shifted ancyromonad ACR enables efficient optogenetic inhibition of pharyngeal activity upon expression in the cholinergic neurons.

Results

Phylogeny and spectral sensitivity

Our bioinformatic search identified ChR homologs in the ancyromonads *Ancyromonas sigmoides, Fabomonas tropica,* and *Nutomonas longa; Ancoracysta twista,* a predatory flagellate placed in the newly established supergroup Provora (Tikhonenkov et al., 2022); the diatom *Odontella aurita*; and *Paraphysoderma sedebokerense*, a chytrid-like fungus from the phylum Blastocladiomycota. Figure 1 – figure supplement 1 shows a protein alignment of their 7TM domains compared with *Gt*ACR1, the best-characterized ACR from the cryptophyte *Guillardia theta* (Govorunova, Sineshchekov, Liu, Janz, & Spudich, 2015; Li et al., 2019). All these sequences exhibit a non-carboxylate residue at the primary counterion (Asp85) position in TM3 of *Halobacterium salinarum* bacteriorhodopsin (BR), marked by the red arrow in Figure 1 – figure supplement 1, as found in all known ACRs. The 2nd carboxylate in the photoactive site, contributed by TM7 and corresponding to Asp212 of BR, is conserved in all these homologs except the one from *N. longa*, in which it is replaced with Glu, and the one from *P. sedebokerense,* in which it is replaced with Gln (the blue arrow in in Figure 1 – figure supplement 1). Phylogenetic analysis placed the ancyromonad ChRs on a separate branch of the ACR tree together with their metagenomic homologs from the TARA Oceans database (Figure 1A). The *A. twista* and *O. aurita* homologs clustered with known stramenopile ACRs. The *P. sedebokerense* sequence showed only a distant homology to previously known ACRs.

We expressed cDNAs encoding the 7TM domains of all these homologs (except the metagenomic homolog) fused to a C-terminal mCherry tag in human embryonic kidney (HEK293) cells and recorded photocurrents using manual patch clamping. All three ancyromonad ChRs generated robust photocurrent and showed maximal sensitivity in the blue spectral range (Figure 1B). Based on their ionic selectivities (see the next section), we named the *A. sigmoides, F. tropica,* and *N. longa* homologs *Ans*ACR, *Ft*ACR, and *Nl*CCR, respectively. Optical manipulation of neuronal activity in dense tissue commonly relies on two-photon (2P) excitation based on the nearly simultaneous absorption of two infrared photons, equivalent to the absorption of one photon in the visible range (Emiliani et al., 2022). The following sections show that *Ans*ACR enables robust optogenetic inhibition of neuronal activity under one-photon (1P) illumination with visible light. We confirmed that *Ans*ACR can also be excited under 2P illumination, with a peak wavelength of ~920 nm (Figure 1C). Next, we expressed the constructs encoding ancyromonad ChRs in *Pichia.* We purified the proteins using a mild detergent yielding 0.25, 0.35, and 0.15 mg purified protein per L culture for *Ans*ACR, *Ft*ACR, and *Nl*CCR, respectively. The absorption spectra of the purified proteins were slightly blue-shifted from the respective photocurrent action spectra (Figure 1D), likely due to the presence of non-electrogenic *cis*-retinal-bound forms.

The spectral sensitivity of the *A. twista* and *O. aurita* homologs was in the blue-green range (Figure 1 – figure supplement 2, left). Partial replacement of Cl^- in the bath with non-permeable aspartate shifted reversal potential (V_r) to more positive values, confirming their anion selectivity (Figure 1 – figure supplement 2, middle and right). We named them *At*ACR, *Oa*ACR1, and *Oa*ACR2. However, their photocurrents were smaller than those of the ancyromonad homologs or exhibited strong desensitization (reduction of photocurrents during illumination), so we did not characterize them in more detail. No photocurrents were detected in cells transfected with the *P. sedebokerense* homolog, although its

expression and membrane targeting were evident from the tag fluorescence. Therefore, we named this protein *Pars*R, where R means "rhodopsin".

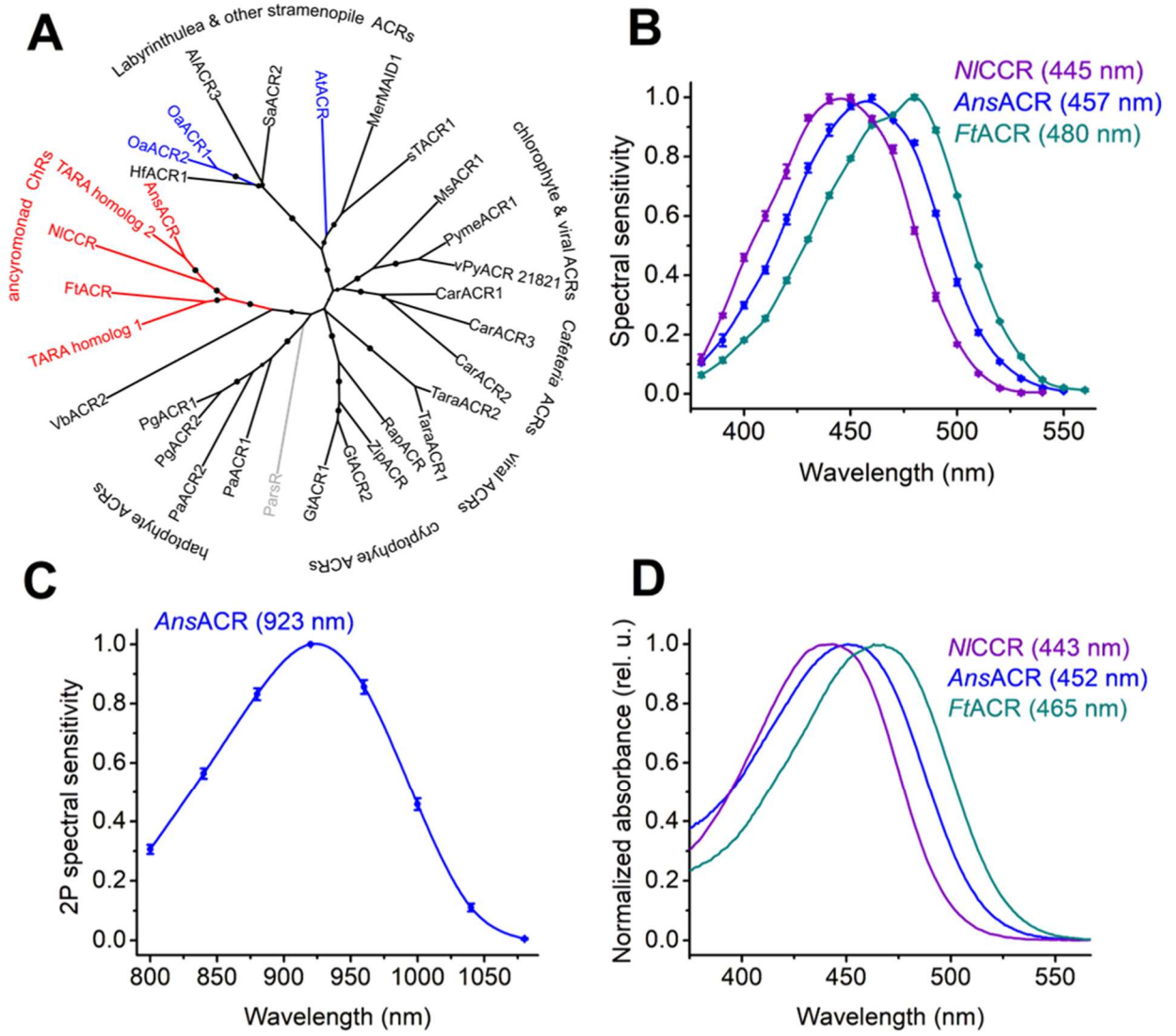

Figure 1. Phylogeny and spectral sensitivity of ancyromonad ChRs.
(**A**) A maximum-likelihood phylogenetic tree of selected ChRs. The circles show bootstrap support from 40 to 100. (**B,C**) The photocurrent action spectra for 1P (B) and 2P (C) excitation. The symbols are the mean values; the error bars are SEM values (for 1P excitation, n = 14 cells for *Ans*ACR, and 9 cells each for *Ft*ACR and *Nl*CCR; for 2P excitation, n = 6 cells). (**D**) The absorption spectra of detergent-purified proteins.

The online version of this article includes the following source data for Figure 1:
Source data 1. Source data for the protein names and accession numbers used to construct the tree in (A); numerical values for the data shown in (B-D).

Characterization of ancyromonad ChRs by automated patch clamping

We used the fully automated planar patch clamp platform SyncroPatch 384 to characterize ancyromonad ChR photocurrents. This instrument uses KF-based internal and NaCl-based external solutions to promote

134 gigaseal formation (Suppl. Table 1). Figure 2A-C shows photocurrent traces evoked by 200-ms light pulses.
135 The SyncroPatch enables unbiased estimation of the photocurrent amplitude because the cells are drawn
136 into the wells without considering their tag fluorescence, unlike manual patch clamp studies in which the
137 experimenter selects the fluorescent cells. Figure 2 – figure supplement 1A, B shows that the mean *Ans*ACR
138 photocurrent measured by the SyncroPatch was significantly larger than the mean *Ft*ACR photocurrent,
139 and *Nl*CCR photocurrent was significantly larger than that of *Platymonas subcordiformis* channelrhodopsin
140 2 (*Ps*ChR2), a previously known excitatory optogenetic tool with a similar blue-shifted spectrum (Chen et
141 al., 2022; Govorunova, Sineshchekov, Li, Janz, & Spudich, 2013).

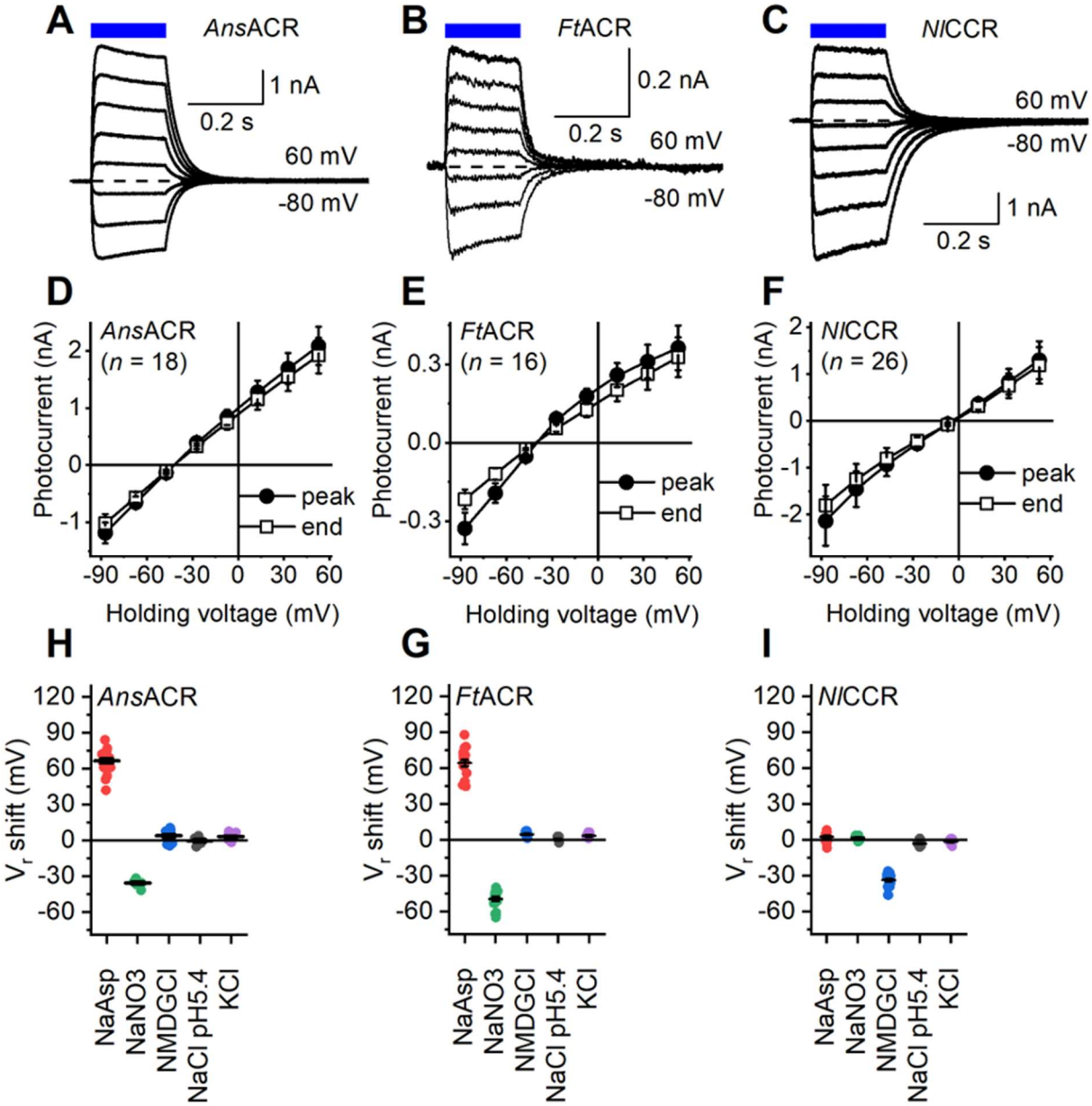

142 **Figure 2. Characterization of ancyromonad ChRs by automated patch clamping.**
143 (**A**) Photocurrent traces recorded in response to 200-ms light pulses (470 nm) at voltages varied in 20-mV
144 steps from -80 mV using the KF-based internal and NaCl-based external solutions. The dashed lines show

the zero-current level. (**B**) The IV curves of the peak current (filled circles) and the current at the end of illumination (empty circles). The numbers in the parentheses are the numbers of cells sampled. (**C**) The V_r values in the indicated external solutions. The circles are the data from individual cells; the lines are the mean and sem values.

The online version of this article includes the following source data for Figure 2:
Source data 1. Source data for the numbers of cells sampled and numerical values shown in (B-C).

The voltage dependencies of photocurrents (IV curves) at the peak time and the end of the light pulse (Figure 2D-F) showed the same reversal potential (V_r), indicating no change in the relative permeability during illumination. *Ans*ACR and *Ft*ACR showed similarly negative V_r values: -43 ± 3 and -41 ± 1 mV, respectively (mean ± sem, n = 22 and 16 cells), suggesting higher relative permeability to Cl^- than F-, as earlier found in *Gt*ACRs by manual patch clamping (Govorunova et al., 2015). Unexpectedly, the *Nl*CCR photocurrents reversed near 0 mV (-1 ± 1 mV, mean ± sem, n = 27 cells). One reason for this behavior could be equal permeabilities of this ChR to Cl^- and F^-. However, when Cl^- in the external solution was partially replaced with bulky, non-permeable aspartate, only *Ans*ACR and *Ft*ACR showed substantial V_r shifts to more positive values (Figure 2G-I, red symbols), which revealed their permeability to Cl^-, but no such shift was detected in *Nl*CCR. Control experiments conducted by manual patch clamping with the Cl^--based pipette solution confirmed these observations (Figure 2 – figure supplement 2). Upon replacing Cl^- with NO_3^-, *Ans*ACR and *Ft*ACR, but not *Nl*CCR, showed V_r shifts to more negative values (Figure 2G-I, green), as did *Gt*ACRs examined by manual patch clamping (Govorunova et al., 2015). *Ft*ACR exhibited a larger V_r shift in NO_3^- than *Ans*ACR (p = 2.6E10-5 by the two-tailed Mann-Whitney test). Replacing Na^+ with N-methyl-D-gluconate ($NMDG^+$) resulted in a negative V_r shift in *Nl*CCR but not the other tested variants (Figure 2G-I, blue symbols), suggesting that *Nl*CCR is permeable to Na^+. Figure 2 – figure supplement 1C, D compares *Nl*CCR with the typical cation-selective *C. reinhardtii* channelrhodopsin 2 (*Cr*ChR2) tested by the same assay. Acidifying the external solution to pH 5.4 or replacing Na^+ with K^+ did not affect the V_r of any ancyromonad ChR (Figure 2G-I, grey and violet). We conclude that only *Ans*ACR and *Ft*ACR are anion-selective, but *Nl*CCR conducts monovalent metal cations despite its sequence homology to the other two variants.

Channel gating and photochemical transitions under single-turnover conditions

Photocurrents evoked by continuous light pulses do not accurately reflect channel kinetics because different ChR molecules absorb photons at different times. Further complications result from photon absorption by photocycle intermediates. We conducted manual patch clamp recordings upon 6-ns laser flash excitation to analyze channel gating. *Ans*ACR and *Ft*ACR photocurrents exhibited biphasic rise and decay (Figure 3A, D), as the earlier characterized *Gt*ACR1 (Sineshchekov, Govorunova, Li, & Spudich, 2015). The IV curves of all kinetic components revealed the same V_r values (Figure 3 – figure supplement 1A, B), meaning no ion selectivity changes occur during the single-turnover photocycle. Next, we analyzed transient absorption changes in detergent-purified *Ans*ACR and *Ft*ACR. In contrast to *Gt*ACR1, we could not find a clear indication of the accumulation of a blue-shifted L intermediate. After an initial (unresolved) decay of a K-like intermediate, red-shifted absorbance temporally increased in both ancyromonad ACRs, reaching a maximum at 100-200 µs (Figure 3B, E, red), i.e., in the time domain of fast channel opening. This red-shifted intermediate could be a long-lived K or an unusual red-shifted L. In *Ft*ACR, an additional slower increase in the red-shifted absorbance likely reflected the formation of an O-like intermediate (Fig. 3E, red). Accumulation of the M intermediate absorbing in the UV range was observed 10 (*Ans*ACR) or 2

times (*Ft*ACR) slower than channel opening (Figure 3C, F), in contrast to *Gt*ACR1, in which it was 50 times slower (Sineshchekov et al., 2015). Unlike *Gt*ACR1, no temporal correlation was found between M formation and fast channel closing and between M decay and slow channel closing in ancyromonad ACRs.

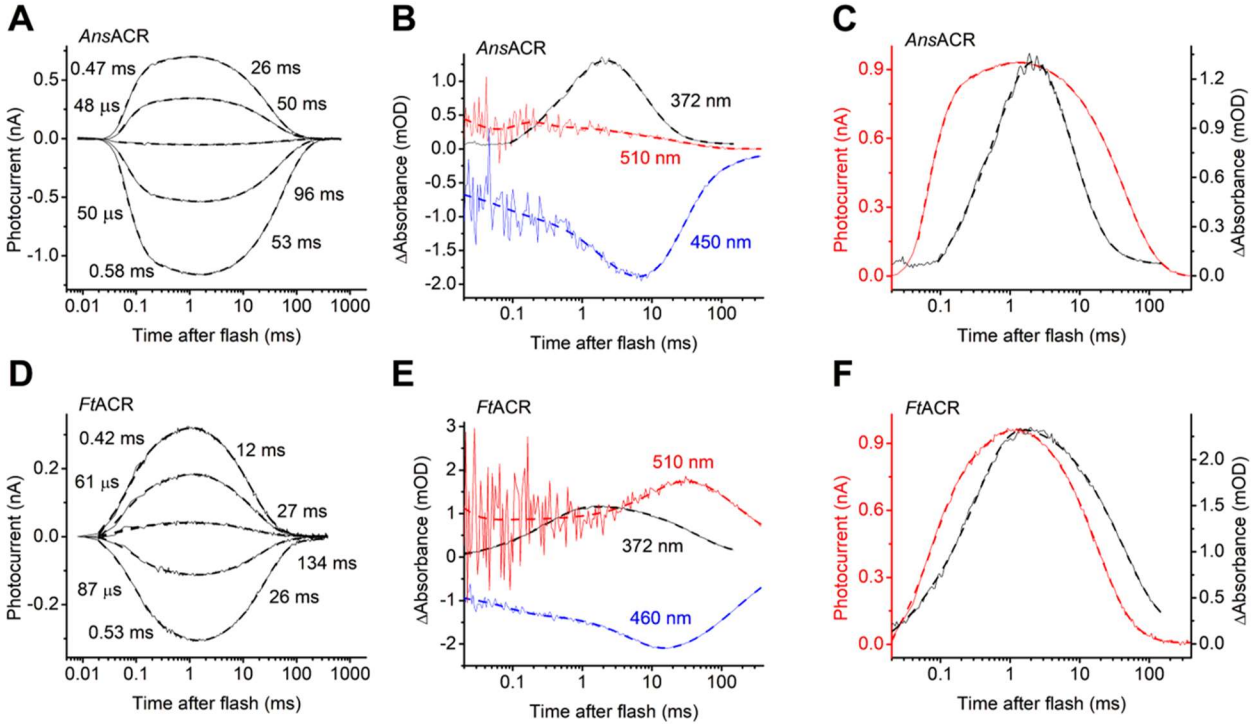

Figure 3. Photocurrent and transient absorption changes under single-turnover conditions in *Ans*ACR and *Ft*ACR. (**A, D**) Photocurrent traces of *Ans*ACR (A) and *Ft*ACR (D) evoked by 6-ns laser flashes recorded by manual patch clamping at the holding voltages increased in 30-mV steps from -60 mV. (**B, E**) Transient absorption changes recorded at the indicated wavelengths from detergent-purified proteins. (**C, F**) Comparison of the photocurrent kinetics (red, left axis) and the M intermediate kinetics (black, left axis). In all panels, the thin, solid lines are experimental recordings, and the thick, dashed lines are multiexponential approximations. The numbers are the τ values of the individual kinetic components.

A pH titration of the peak wavelength (λ_{max}) (Figure 4A, black filled circles, left axis) or maximal absorption changes (Figure 4A, black empty circles, right axis) in the wild-type *Ans*ACR revealed the main transition with a pK_a 4. The 4-nm redshift of λ_{max} observed in the wild type (WT) upon acidification corresponded to the ~8 nm redshift of the photocurrent action spectrum of the *Ans*ACR_D226N mutant relative to the WT (Figure 4B). Therefore, we conclude that this spectral transition in the WT reflects the titration of the counterion Asp226. Photocurrent in the *Ans*ACR_D226N mutant was not much affected, but its rise and decay became monophasic (Figure 4C). Furthermore, the monophasic decay in this mutant accelerated upon depolarization, in contrast to both decay phases in the WT (Figure 4D.

All ACRs have a non-carboxylate residue in the position of Asp85 in BR (Figure 1 – figure supplement 1, red arrow). Mutagenetic introduction of Glu in this position in *Ans*ACR (the G86E mutation) caused a new pH-induced spectral transition with a pK_a of 7.4 and a shift of the pK_a in the acidic range from 4.0 to 4.7 (Figure 4A, red). This mutation also led to the appearance of an extremely fast (τ 31 µs) M-like UV-absorbing intermediate (Figure 4E, red). Most importantly, this mutation eliminated channel current at neutral pH

210 and led to the appearance of a fast current. The rise and decay τ of the latter corresponded to the rise and
211 decay τ of fast M formation (compare Figures. 4E and F). Acidification of the bath to pH 5.4 recovered
212 channel current (Figure 4F, red), the kinetics of which differed from that in the WT (Figure 3A). The full
213 current trace could be deconvoluted into four components with τ 30 µs, 80 µs, 1.5 ms, and 640 ms,
214 revealing that the mutation slowed channel closing 6-fold. Replacement of Cl^- with Asp^- caused a~40-mV
215 shift of the channel current's V_r (Figure 3 – figure supplement 1C), indicating that the mutant channel
216 remained Cl^- selective. Acidification increased the amplitude of the fast current ~10-fold (Figure 4F) and
217 shifted its V_r ~100 mV (Figure 3 – figure supplement 1D), as expected of passive proton transport. The
218 number of charges transferred during the fast peak current was >2,000 times smaller than during the
219 channel opening, from which we concluded that the fast current reflects the movement of the RSB proton.
220 Similar τ values of the fast current decay and the decay of fast M formation (Figures 4E and F) corroborate
221 this conclusion. These results confirm that the absence of a negative charge at BR's primary acceptor site
222 is the ultimate condition for anion channel function. The glutamate in the middle of TM2 corresponding
223 to Glu68 of *Gt*ACR1 is conserved in most ACRs, including *Ft*ACR, but replaced with Gln in *Ans*ACR (Figure
224 1 – figure supplement 1, black arrow). The Q48E mutation in AnsACR accelerated channel closing and
225 slowed channel opening, making the photocurrent rise and decay monophasic (Figure 4G, Figure 3 – figure
226 supplement 1E).

227 In contrast to *Natronomonas pharaonis* halorhodopsin (Varo, Brown, Needleman, & Lanyi, 1996), no blue
228 spectral shift was detected in detergent-purified *Ans*ACR upon an increase in the Cl^- concentration (Figure
229 4 – figure supplement 4A), which argued against Cl^- binding in the RSB region at neutral pH. Strong
230 alkalization caused simultaneous depletion of absorption in the visible range, the appearance of the M-
231 like states (at 368 nm in the wild-type *Ans*ACR and 355 nm in the *Ans*ACR_G86E mutant), and a substantial
232 absorption increase at 297 nm, reflecting deprotonation of the RSB and a strong perturbation of the
233 protein band (Figure 4 – figure supplement 1B). Analysis of the pH dependence of three parameters
234 (absorption depletion in the visible range, absorption rise in the M-like states' range, and absorption rise
235 at 297 nm) yielded similar pK_a values, which were 11.1 and 10.7 for the WT and G86E, respectively (Figure
236 4 – figure supplement 1C). These high pK_a values may explain high photostability of this protein, as
237 hundreds of laser flashes did not cause its measurable bleaching.

238 In contrast to *Ans*ACR and *Ft*ACR, only two exponentials were sufficient to fit *Nl*CCR laser-flash-evoked
239 photocurrents, both in Cl^- and Asp^- bath solutions (Figure 4H, Figure 3 – figure supplement 1F). We
240 conducted pH titration of its stationary absorption (Figure 4I). From analogy with *Ans*ACR, we interpret
241 the spectral transition with pK_{a1} 3.4 as protonation of the residue corresponding to Asp212 in BR, which is
242 Glu233 in *Nl*CCR (Figure 1 – figure supplement 1, blue arrow). Upon further acidification, *Nl*CCR exhibited
243 a second large transition to shorter wavelengths with pK_{a2} 1.1, only slightly presented in ancyromonad
244 ACRs. A similar transition was observed in haloarchaeal rhodopsins and explained by Cl^- binding in the
245 photoactive site (Shimono, Kitami, Iwamoto, & Kamo, 2000).

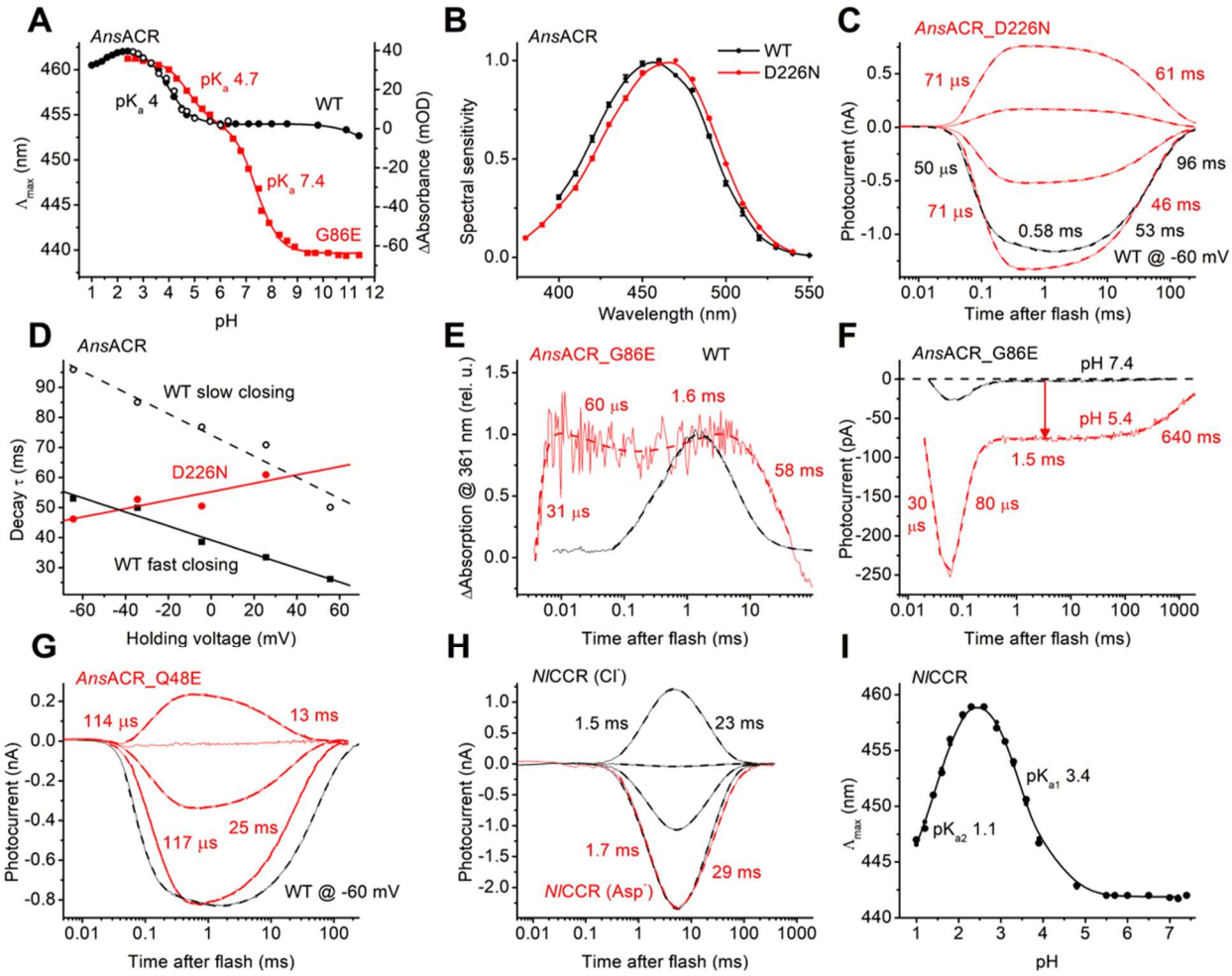

Figure 4. Characterization of the wild-type proteins and *Ans*ACR mutants.

(**A**) pH titration of λ_{max} (black filled circles, left axis) and maximal absorption changes (black empty circles, right axis) in wild-type *Ans*ACR, and λ_{max} in *Ans*ACR_G86E mutant (red, left axis). (**B**) The photocurrent action spectrum of the *Ans*ACR_D226N mutant (red) compared to the WT (black). The symbols are the mean values, and the error bars are SEM values (n = 8 cells). (**C, G**) Photocurrent traces of *Ans*ACR_D226N mutant (C) and *Ans*ACR_Q48E mutant (G) evoked by 6-ns laser flashes recorded by manual patch clamping at the holding voltages increased in 30-mV steps from -60 mV. The wild-type photocurrent trace recorded at -60 mV is shown in black for comparison. The thin lines are experimental recordings, and the thick dashed lines are multiexponential approximations. The numbers are the τ values of the individual kinetic components. (**D**) The voltage dependence of the decay components τ in the *Ans*ACR_D226N mutant (red) and the WT (black). (**E**) Transient absorption changes monitored at the wavelength of the M intermediate absorption in the *Ans*ACR_G86E mutant (red) compared to the WT (black). (**F**) Laser-flash-induced photocurrents of the *Ans*ACR_G86E mutant recorded at the external pH 7.4 (black) and 5.4 (red). The arrow shows the increase in the channel current upon acidification. (**H**) Laser-flash evoked photocurrent traces of *Nl*CCR recorded at the holding voltages increased in 30-mV steps from -60 mV using the Cl^--(black) or Asp^--based (red) bath solution. (**I**) pH titration of detergent-purified *Nl*CCR.

The online version of this article includes the following source data for Figure 4:

Source data 1. Source data for the numerical values shown in (A, B, D, and I).

The retinal-binding pocket and color tuning

The λ_{max} of rhodopsins is regulated by the retinal chromophore geometry and steric and electrostatic interactions of the chromophore with amino acid residues of the retinal-binding pocket (Hoffmann et al., 2006; Karasuyama, Inoue, Nakamura, Kandori, & Takeuchi, 2018). Surprisingly, *Nl*CCR, the most blue-shifted among ancyromonad ChRs, features three residues typical of red-shifted microbial rhodopsins (Figure 5A). The first is Phe at the primary counterion position (Asp85 in BR), also found in RubyACRs from Labyrinthulea, the most red-shifted ChRs so far identified (Govorunova et al., 2020). The residues homologous to BR's Met118 near the β-ionone ring and Ala215 preceding the RSB lysine in the polypeptide chain are responsible for red-shifted absorption in many microbial rhodopsins (Engqvist et al., 2015; Oda et al., 2018; Oppermann et al., 2024; Shimono, Iwamoto, Sumi, & Kamo, 2000) but are conserved in all three blue-absorbing ancyromonad ChRs. In *Gt*ACR1 (λ_{max} 515 nm, (Govorunova et al., 2015; Sineshchekov, Li, Govorunova, & Spudich, 2016)), the only ACR with published atomic structures (Kim et al., 2018; Li et al., 2019), the corresponding residues are Ser97, Cys133, and Cys237 (Figure 5B). As expected, the S97F, C133M, and C237A mutations red-shifted the *Gt*ACR1 spectrum (Figure 5C). The opposite F104S, M143C, and A242C mutations at the corresponding sites in the RubyACR from *Hondaea fermentalgiana* (*Hf*ACR1) caused large blue spectral shifts (Figure 5D). However, the corresponding mutations F85S, M141C, and A236C red-shifted the *Nl*CCR spectrum (Figure 5E). The same paradoxical behavior was observed upon mutation of the Met118 homolog to Val, which blue-shifted the *Hf*ACR1 spectrum but red-shifted the ancyromonad ChR spectra (Figure 5F-H). Replacement of the Ala215 homolog with Cys or Ser did not change the *Ans*ACR and *Ft*ACR spectra (Figure 5 – figure supplement 1A, B).

In blue-shifted ChRs such as *Platymonas subcordiformis* channelrhodopsin 2 (*Ps*ChR2) (Govorunova et al., 2013) and *Klebsormidium nitens* channelrhodopsin (*Kn*ChR) (Tashiro et al., 2021), the position of BR's Met118 is occupied by Gly or Ala (Figure 5A), which, together with the Ala four residues downstream (BR's Gly122), rotates the β-ionone ring out of the plane of the polyene chain, shrinking the *p*-conjugation and blue-shifting the spectrum (Wang et al., 2024). This Ala is conserved in *Ans*ACR and *Nl*CCR (Figure 5A), but the *Ans*ACR_M134A/G and *Nl*CCR_M141A/G mutations did not change the spectra, nor did the *Ft*ACR_M140G_V144A mutation (Figure 5 – figure supplement 1A-C). These observations suggest that the residue geometry and/or interactions in the retinal-binding pocket in ancyromonad ChRs differ from the earlier studied microbial rhodopsins.

The residue position corresponding to BR's Leu93 is the color switch between blue- and green-absorbing proteorhodopsins (BPRs and GPRs, (Man et al., 2003)). *Ans*ACR exhibits a Gln residue in this position, as do BPRs, but *Ft*ACR has Leu, as do GPRs, and *Nl*CCR has Met (Figure 5A). The *Ft*ACR_L96Q and *Nl*CCR_M93Q mutations blue-shifted the spectra 20 and 7 nm, respectively (Figure 5I, J), indicating that this residue position contributes to color tuning in ancyromonad ACRs. *Nl*CCR, the most blue-shifted among ancyromonad ChRs, differs from *Ans*ACR and *Ft*ACR at the positions corresponding to Ser89 and Glu233 (*Nl*CCR numbering), and from *Ft*ACR, also at the position of Pro235 (the corresponding residues in *Gt*ACR1 are Thr101, Asp234, and Leu236, Figure 5A). The S89T, E233D, and P235I mutations red-shifted the *Nl*CCR spectrum (Figure 5K), indicating that these three positions contribute to the blue shift of wild-type *Nl*CCR compared to *Ans*ACR and *Ft*ACR. However, the T90S mutation did not change the *Ans*ACR

303 spectrum, and the D226E mutation and a combination of the two mutations caused red spectral shifts in
304 *Ans*ACR (Figure 5 – figure supplement 1D).

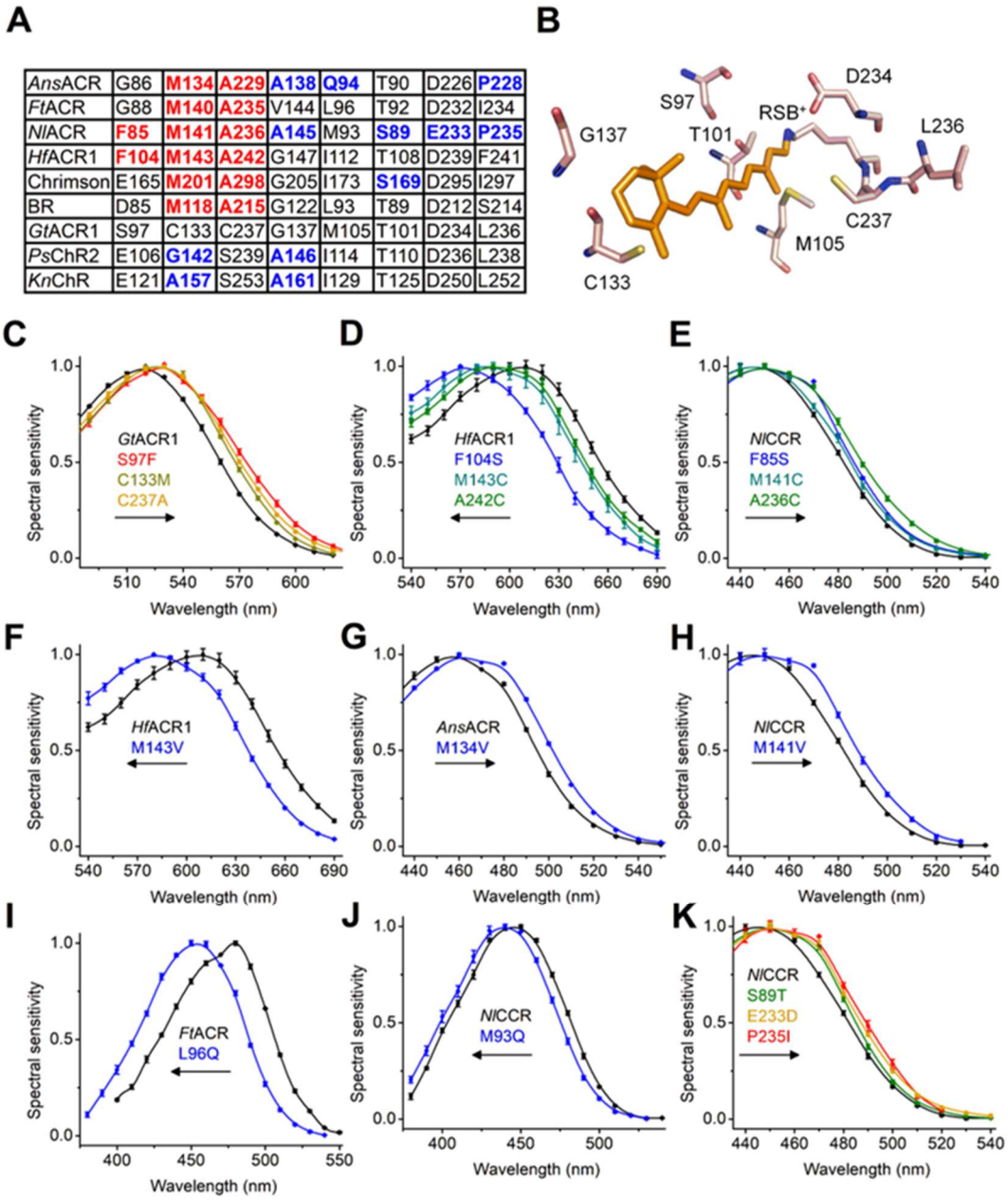

305 **Figure 5. Color tuning of ancyromonad ChRs.**
306 (**A**) Amino acid residues of the retinal-binding pocket tested by mutagenesis in this study. (**B**) The
307 corresponding residues in the *Gt*ACR1 structure (6edq). (**C-K**) The photocurrent action spectra of the
308 indicated mutants compared to the respective WTs. The symbols are the mean values, the error bars are
309 SEM values.

310 The online version of this article includes the following source data for Figure 5:
311 Source data 1. Source data for the numbers of cells sampled and numerical values shown in (C-K).

Optogenetic inhibition of cortical neurons in mouse brain slices

To test the silencing efficiencies of *Ans*ACR and *Ft*ACR in mice, we selectively expressed their 7TM domains fused with EYFP in the layer 2/3 pyramidal neurons of the somatosensory cortex by *in utero* electroporation at embryonic day 15. Bright fluorescence was observed in the somata, dendrites, and axons, indicating high-level *Ans*ACR-EYFP and *Ft*ACR-EYFP expression (Figure 6 – figure supplement 1A). We prepared acute brain slices from 4-6-week-old mice and performed whole-cell current clamp recordings from *Ans*ACR- or *Ft*ACR-expressing neurons (for solution compositions, see Material and Methods). *Ans*ACR- and *Ft*ACR-expressing neurons showed the resting membrane potential, input resistance, and capacitance values within the range typical of untransfected cortical neurons (Figure 6 – figure supplement 1B), suggesting that expression of these ACRs induced negligible cytotoxicity. When positive currents were injected into the somata to excite neurons, photoactivation of *Ans*ACR and *Ft*ACR suppressed the current-evoked action potentials, demonstrating the potency of these proteins as optogenetic silencers of mouse cortical neurons (Figure 6). We also observed that at rest or when a small negative current (e.g., -0.1 nA) was injected, the neurons could generate a single action potential at the beginning of photostimulation (Figure 6A, B), similar to *Gt*ACR-expressing neurons (Mahn et al., 2018; Messier, Chen, Cai, & Xue, 2018).

Earlier studies have shown that photoactivation of *Gt*ACRs induces axonal depolarization and synaptic transmission in some ACR^+ neurons owing to the high intracellular Cl^- concentration at the axons (Mahn et al., 2018; Messier et al., 2018). Indeed, when we recorded from ACR^- neurons in the electroporated cortical region, we found that photoactivation of either *Ans*ACR- or *Ft*ACR-induced excitatory post-synaptic currents (Figure 6 – figure supplement 1C, D) similar to other tested light-gated Cl^- channels.

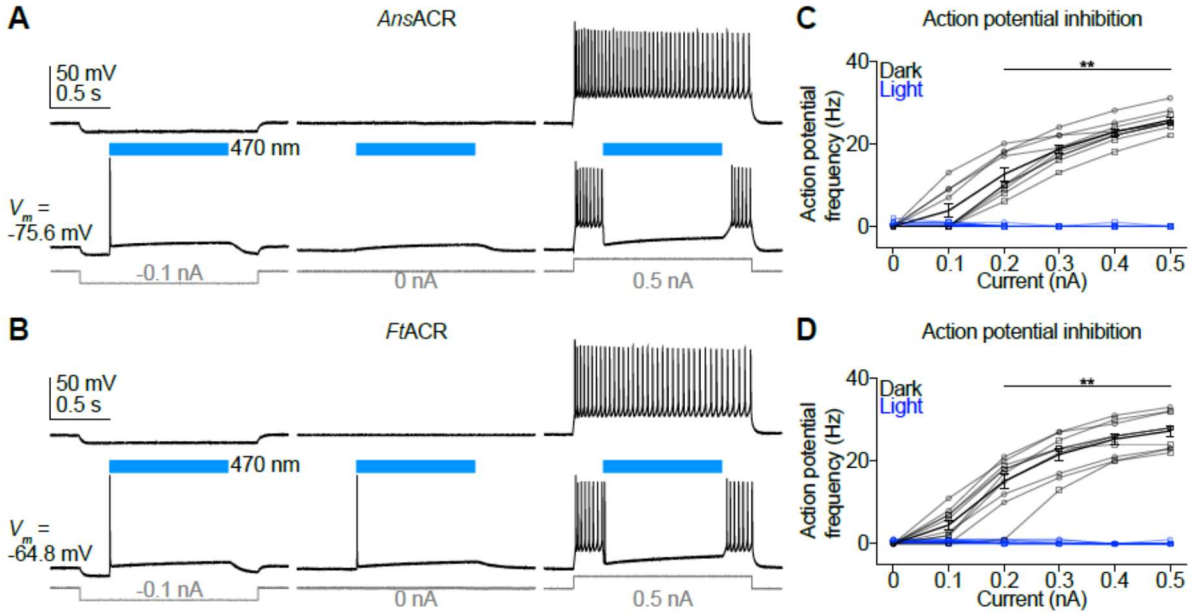

Figure 6. Photoactivation of *Ans*ACR and *Ft*ACR inhibits the action potentials of mouse cortical neurons. (**A, B**) Representative membrane voltage traces of neurons expressing *Ans*ACR (A) and *Ft*ACR (B) in response to -0.1 nA (left), 0 nA (middle), and 0.5 nA (right) injections without (top) and with (bottom) 470 nm light pulses (power density of 38.7 mW mm^{-2}). (**C, D**) The frequencies of action potentials evoked by different current injections with (blue) and without (black) photoactivation of *Ans*ACR (C) and *Ft*ACR (D).

For all panels, data points from male mice are indicated by squares and female mice by circles. One male and one female mouse were used for each of the *Ans*ACR and *Ft*ACR experiments. Data are mean ± sem. **, $p \leq 0.01$ for 0.2-0.5 nA by the multiple Wilcoxon matched-pairs signed rank test with Benjamini, Krieger, and Yekutieli's corrections.

The online version of this article includes the following source data for Figure 6:
Source data 1. Source data for the numerical values shown in (C, D).

Optogenetic inhibition of pharyngeal function in live C. elegans

To test *Ans*ACR as an optogenetic inhibitory tool in the context of an intact behaving animal, we expressed the encoding construct fused to a C-terminal EYFP tag in the *C. elegans* cholinergic neurons using the *unc-17* promoter (a scheme of the expression construct is shown in Figure 7A). To assess pharyngeal function non-invasively, we recorded EPGs from live animals sucked into a pipette (Raizen & Avery, 1994). An EPG contains transients reflecting pharyngeal muscle action potentials (Figure 7B), the frequency of which can be easily quantified. In the presence of 10 mM serotonin required to maintain regular pharyngeal pumping, its frequency in the dark was not significantly different in the transgene and wild-type worms (4.07 ± 0.05 and 4.19 ± 0.08 Hz, respectively, mean ± SEM, n = 26 transgenic and 11 wild-type worms, respectively; the p-value by the two-tailed Mann-Whitney test is 0.21), indicating that *Ans*ACR expression did not affect the pharyngeal function in the darkness. Figure 7C shows representative EPG recordings from a transgenic worm fed on bacteria supplemented with all-*trans*-retinal. The onset of 470-nm illumination caused an immediate inhibition of pumping in such transgene worms but not in the WT worms fed on the same bacteria or transgene worms in the absence of retinal (Figure 7D). The *C. elegans* genome encodes LITE-1 and GUR-3 UV/blue light receptors (unrelated to ChRs) responsible for photoinhibition of pharyngeal pumping at high light levels (Bhatla & Horvitz, 2015). However, no photoinhibition was detected in the absence of retinal in either wild-type or transgenic worms. This indicates that the irradiance used in our experiments was insufficient to stimulate these endogenous photoreceptors. The magnitude of the *Ans*ACR-mediated photoinhibition depended on the irradiance (Figure 7E). The maximal irradiance (2.1 mW mm^{-2}) completely abolished the pumping for 15 s in all tested worms (n = 13). In five of 13 worms, individual action potentials were observed during the second half of the 30-s illumination period, an indication of adaptation. Two independently created transgenic lines showed the same degree of photoinhibition (Figure 7E, filled and empty symbols). The photoinhibition was fully reversible: after switching off the maximal-irradiance light, the pumping frequency returned to the pre-illumination level with τ ~9 s.

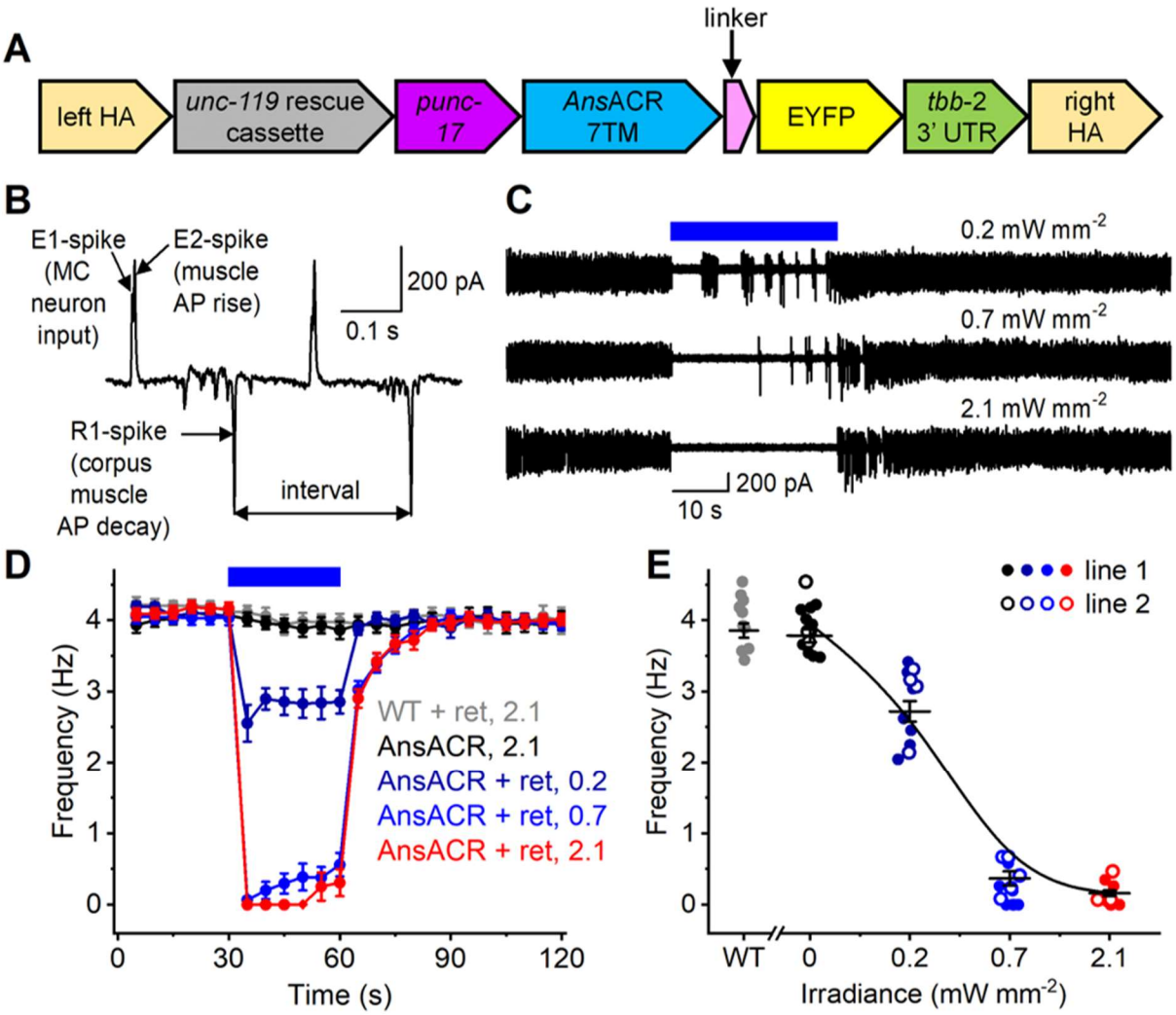

Figure 7. Photoinhibition of pharyngeal pumping in live *C. elegans* expressing *Ans*ACR in the cholinergic neurons.

(**A**) A scheme of the genetic construct for *Ans*ACR expression in the cholinergic neurons. HA, homology arms. (**B**) A zoomed-in section of an EPG recording. AP, action potential; TB, terminal bulb. The double-headed arrow shows the interval between two successive R1 spikes used to calculate pharyngeal pumping frequency. (**C**) Electropharyngeogram recordings from an *Ans*ACR-expressing worm illuminated with 470 nm light at the indicated irradiances. The blue bar shows the duration of illumination. (**D**) The frequency of the pharyngeal pumping calculated from recordings as shown in A. The symbols are the mean values, and the error bars are the SEM values (n = 11 worms for the WT and 13 worms per condition for the transgenic worms). The numbers are the irradiance values in mW mm^{-2}; ret is the abbreviation for retinal. (**E**) The dependence of the pharyngeal pumping frequency on the irradiance calculated from the 30-60 s segment of the data shown in B. The symbols are the data from individual worms; the lines are the mean and SEM values. The empty and filled symbols for the transgenic worms show the data from two independently created transgenic lines.

The online version of this article includes the following source data for Figure 6:
Source data 1. Source data for the numerical values shown in (D, E).

Discussion

ChRs, also known as "*Chlamydomonas* sensory rhodopsins," were first discovered as the photoreceptors guiding phototaxis and the photophobic response in the chlorophyte *C. reinhardtii* (Govorunova, Jung, Sineshchekov, & Spudich, 2004; Sineshchekov et al., 2002). Since then, ChRs have been identified in the genomes and transcriptomes of several other eukaryotic supergroups, including cryptophytes, haptophytes, stramenopiles, and alveolates (Govorunova et al., 2021; Govorunova et al., 2020; Govorunova et al., 2015). Furthermore, ChRs appear in the genomes of giant viruses, which likely facilitate the spread of ChR genes by horizontal transfer (Rozenberg et al., 2020; Zabelskii et al., 2020). Our identification and characterization of ChRs in ancyromonads, phylogenetically placed near the most commonly inferred root of the eukaryote tree (Brown et al., 2018), suggests that eukaryotes acquired ChR genes at the early steps of their evolution. Consistent with the role of the encoded proteins as phototaxis receptors directly proven in *C. reinhardtii*, ChR genes or transcripts occur only in protists that develop flagella at some stage of their life cycle. No exception is the diatom *O. aurita*, in which we also identified ChRs: flagella are lost in the vegetative state of this protist but are still present in its male gametes (Nanjappa, Sanges, Ferrante, & Zingone, 2017).

Prediction of biophysical properties such as ionic selectivity from protein sequences is a major unresolved problem in ChRs research. The *Nl*CCR sequence shows ~29% identity and ~49% similarity in the 7TM domain to each of the two ancyromonad ACRs and contains a neutral residue in the counterion position (Asp85 in BR), typical of all ACRs (Figure 1 – figure supplement 1, red arrow). Yet, *Nl*CCR does not conduct anions, showing instead permeability to Na^+. In the earlier known ChRs, the presence of conserved Glu residues in TM2 and the TM2-TM3 loop, corresponding to Glu82, Glu83, Glu90, and Glu101 of *Cr*ChR2, correlates with cation selectivity (Govorunova et al., 2021). However, TM2 of *Nl*CCR contains no carboxylated residues (Figure 1 – figure supplement 1), which suggests a unique mechanism of cation selection in this channel. *Nl*CCR is the most blue-shifted among ancyromonad ChRs and generates larger photocurrents than the earlier known CCRs with a similar absorption maximum (Govorunova et al., 2013), which makes it a good candidate for optogenetic stimulation of neuronal activity.

All ancyromonad ChRs absorb light in the blue spectral range. The λ_{max} of retinylidene proteins is determined by the energy gap between the electronic ground (S0) and first excited (S1) state of the chromophore, dependent on the chromophore geometry, the protonation state of the Schiff base counterion, and the interaction of the chromophore with other residues of the retinal-binding pocket (Engqvist et al., 2015; Ernst et al., 2014; Kato et al., 2015). Paradoxically, the retinal-binding pockets of all three ancyromonad ChRs contain the residues corresponding to Met118 and Ala215 of bacteriorhodopsin, the well-known "color switches" characteristic of red-shifted microbial rhodopsins. The role of the near-ring Met118 homolog in red-shifting the spectrum has been experimentally verified in *Haloquadratum walsbyi* BR (Sudo et al., 2013), *Gloeobacter violaceus* rhodopsin (Engqvist et al., 2015), archaeorhodopsin-3 (Kato et al., 2015), and Chrimson (Oda et al., 2018). It is thought that the bulky Met side chain pushes away the C7 atom of retinal, increasing the ring-chain coplanarity, expanding the π conjugation, and red-shifting absorbance, as theoretically predicted in the *Gt*ACR1_C133M mutant (Tsujimura et al., 2021). The red-shifting effect of the Ala215 homolog has been demonstrated in *N. pharaonis* sensory rhodopsin II (K. Shimono et al., 2000), *H. salinarum* BR (Spudich et al., 2012), Chrimson (Oda et al., 2018), sodium-pumping rhodopsin KR2 (Inoue et al., 2019), and *Mantoniella squamata* ACR1 (Oppermann et al., 2024), and is explained by electrostatic interactions between the polar residue in this position and the RSB. However, in ancyromonad ChRs, mutations of the Met118 homolog to smaller residues and the Ala215 homolog to

428 polar residues caused a red rather than blue spectral shift or no shift. Furthermore, the mutagenetic
429 introduction of the ring-rotating residues responsible for the blue-shifted spectra of *Hyphochytrium*
430 *catenoides* kalium channelrhodopsin 2 (Tajima et al., 2023) and *Kn*ChR (Wang et al., 2024) did not change
431 the ancyromonad ChR spectra, which suggests that either the torsion around the C6-C7 bond is already
432 enforced by a different geometry of the Met118 homolog or that their blue-shifted absorbance arises by
433 a different mechanism. Atomic structures of ancyromonad ChRs are needed to investigate their
434 paradoxical retinal binding pockets and the reasons for their unusual spectral properties.

435 ACRs are widely used to inhibit neuronal activity with light. We evaluated *Ans*ACR and *Ft*ACR as neuronal
436 silencers in mouse brain slices and *Ans*ACR in the context of a live animal, the nematode *C. elegans*. We
437 previously showed that *Gt*ACRs could inhibit action potentials at the soma while triggering synaptic
438 transmission due to high axonal Cl^- reversal potential (Messier et al., 2018). *Ans*ACR and *Ft*ACR showed
439 similar phenomena in our brain slice experiments. These ACRs can inhibit action potentials in cortical
440 neurons but depolarize axonal terminals and trigger synaptic transmission. Fusing these new ACRs with
441 somatodendritic trafficking motifs to reduce axonal expression (Mahn et al., 2018; Messier et al., 2018)
442 could lead to potent inhibition with reduced axonal excitation.

443 Optogenetic inhibition of *C. elegans* pharyngeal pumping has been demonstrated earlier upon expression
444 of the *Leptosphaeria maculans* proton-pumping rhodopsin known as Mac (Trojanowski, Padovan-Merhar,
445 Raizen, & Fang-Yen, 2014) or *N. pharaonis* halorhodopsin (*Np*HR) (Schüler, Fischer, Shaltiel, Steuer Costa,
446 & Gottschalk, 2015) in the cholinergic neurons. However, ion-pumping rhodopsins such as these transport
447 only one ion per absorbed photon and, therefore, require almost 20 times higher irradiance for
448 photoinhibition than the maximal irradiance used in this study. All ACRs, including *Ans*ACR that we tested
449 in the worms, transport multiple anions during the open state and, therefore, are more efficient
450 optogenetic silencers than the ion-pumping rhodopsins. The partial recovery of pharyngeal pumping that
451 we observed after 15-s illumination, even at the highest tested irradiance, most likely reflects an
452 adaptation of the pharyngeal muscles capable of generating autonomous contractions in the presence of
453 acetylcholine tonically released from the pharyngeal neurons (Trojanowski et al., 2016).

454 *Ans*ACR exhibited robust 2P excitation, with action spectra showing a maximum at ~920 nm. This
455 wavelength aligns well with the excitation range of common Ti:Sapphire lasers, widely used in
456 neuroscience laboratories. These findings show that *Ans*ACR can be deployed for *in vivo* optogenetic
457 silencing with single-cell or subcellular precision, expanding the toolkit for precise manipulations in
458 neuroscience research. Our characterization of ancyromonad ChRs has contributed to a better
459 understanding of light-gated channel function and yielded superior blue-shifted tools for optogenetic
460 excitation and inhibition.

461 **Materials and Methods**

462 *Bioinformatics and molecular biology*

463 The ChR homologs from *Ancyromonas sigmoides* strain B-70 (CCAP1958/3), *Fabomonas tropica* strain
464 NYK3C, *Nutomonas longa* strain CCAP 1958/5 (Brown et al., 2018; Torruella et al., 2015), and *Ancoracysta*
465 *twista* strain TD-1 (Janouškovec et al., 2017) were identified in the EukProt V3 database (Richter et al.,
466 2022) using Sequnceserver BLASTP (Priyam et al., 2019). The *A. sigmoides*, *F. tropica*, and *A. twista* ChR
467 sequences are available from Dr. Andrey Rozenberg's ChR database (Rozenberg, 2024). The metagenomic
468 homolog 1 was found by Sequnceserver BLASTP in the TARAeuCatV2 database (Sunagawa et al., 2015)

469 accessed at the KAUST Metagenomic Analysis Platform (KMAP) (Alam et al., 2021). The metagenomic
470 homolog 2 was found using the search mode of BLASTP in the MATOU database (Marine Atlas of Tara
471 Oceans Unigene plus metaG eukaryotes) (Villar et al., 2018) with the query sequence of *Nl*CCR. The
472 *Odontella aurita* strain CCMP816 homologs GHBW01284417 and GHBW01118808 were identified by
473 TBLASTN in the National Center of Biological Information (NCBI) transcriptome shotgun assembly (TSA)
474 project GHBW00000000. The *Paraphysoderma* homolog (*Pars*R) was found in the *P. sedebokerense* strain
475 JEL821 v. 1.0 genome assembly (Amses et al., 2022) by the annotation text search using bacteriorhodopsin
476 as a keyword at the Mycocosm portal (Grigoriev et al., 2014).

477 The protein alignment was created using the MUSCLE algorithm with default parameters implemented in
478 MegAlign Pro software v. 17.1.1 (DNASTAR Lasergene, Madison, WI) and truncated after the end of TM7.
479 Phylogeny was analyzed with IQ-TREE v. 2.1.2 (Minh et al., 2020) using automatic model selection and
480 ultrafast bootstrap approximation (1,000 replicates) (Hoang, Chernomor, von Haeseler, Minh, & Vinh,
481 2018). The best tree was visualized and annotated using iTOL v. 7 (Letunic & Bork, 2024).

482 For expression in human embryonic kidney (HEK293) cells, mammalian codon-optimized polynucleotides
483 encoding amino acid residues 1-265 of the *A. sigmoides* homolog, 1-268 of the *F. tropica* homolog, 1-272
484 of the *N. longa* coding homolog, 1-243 of the *A. twista* homolog, 1-241 of the GHBW01284417 *O. aurita*
485 homolog, 1-242 of the GHBW01118808 *O. aurita* homolog, and 1-336 of the *P. sedebokerense* homolog
486 were synthesized, fused to a C-terminal mCherry tag, and cloned into the pcDNA3.1(+) vector (Invitrogen,
487 Cat. #V19520) at GenScript. For expression in *Pichia*, the constructs were fused with the C-terminal 8His-
488 tag and cloned in the pPICZalpha-A vector (Invitrogen, Cat. #V19520). A QuikChange XL site-directed
489 mutagenesis kit (Agilent Technologies, Cat. #200516) was used to introduce point mutations. For
490 expression in the mouse cortical neurons, *Ans*ACR and *Ft*ACR were tagged with EYFP (enhanced yellow
491 fluorescent protein) at the C-terminus and cloned into the pAAV-CAG vector.

492 *HEK293 cell culture and transfection*

493 No cell lines from the list of known misidentified cell lines maintained by the International Cell Line
494 Authentication Committee were used in this study. HEK293 cells used in 1P excitation experiments were
495 obtained from the American Type Culture Collection (ATCC; Cat. #CRL-1573). The cells were plated on 2-
496 cm diameter plastic dishes 48-72 hrs before experiments, grown for 24 hrs, and transfected with 10 µl of
497 Lipofectamine LTX with Plus Reagent (ThermoFisher, Cat. #15338100) using 3 µg DNA per dish for manual
498 patch clamping, and 6 µg DNA per dish for automated patch clamping. All-*trans*-retinal (Millipore-Sigma,
499 Cat. #116-31-4) was added immediately after transfection at the final concentration of 5 µM. For 2P
500 excitation experiments, HEK293A cells were plated on 30-70 kDa poly-*d*-lysine-coated 12-mm circular
501 coverslips (Carolina cover glass #0, Cat. #633009) in 24-well plates (P24-1.5H-N, Cellvis) at 30% confluence,
502 transfected with 1.2 µL FuGENE HD transfection reagent (Promega, Cat. #E2311) using 200 ng DNA per
503 well 48-72 h before measurements, and supplemented with all-*trans*-retinal as described above.

504 *Automated whole-cell patch clamp recording from HEK293 cells*

505 Automated patch clamp recording was conducted at room temperature (21°C) 48-72 h after transfection
506 with a SyncroPatch 384 (Nanion Technologies) based on a Biomek i5 automated liquid handler (Beckman
507 Coulter), using NPC-384T S-type chips (Nanion, Cat. #222101) with one hole per well, as described earlier
508 (Govorunova, Sineshchekov, Brown, & Spudich, 2022). Before measurements, transfected cells were
509 dissociated using TrypLE Express, diluted with CHO-S-SFM-II medium (both from ThermoFisher, Cat.#

510 12604013 and 31033020, respectively) and resuspended in External Physiological solution (Nation, Cat.#
511 08 3001). The compositions of this and other solutions used in automated patch clamp recordings and the
512 corresponding liquid junction potential (LJP) values calculated using the ClampEx LJP calculator are listed
513 in Supplementary Table 1. The voltages in all IV curves for HEK293 cells in this manuscript were corrected
514 for LJPs; the holding voltage values in the figures showing traces correspond to the amplifier output before
515 the LJP subtraction. Illumination was provided with LUXEON Z Color Line light-emitting diodes (LEDs) Cat.#
516 LXZ1-PB01 (470 ± 10 nm) arranged in a 6×16 matrix. The forward LED current was 900 mA, the illumination
517 duration was 200 ms (limited by the LED duty cycle), and the interval between successive light pulses was
518 60 s. The LEDs were driven by a derivative of CardioExcyte 96 SOL (Nanion, Cat. #191003) and controlled
519 by Biomek commands. PatchControl384 v. 2.3.0 (Nanion Technologies) software was used for data
520 acquisition at a 5 kHz sampling rate (200 µs per point). The photocurrent amplitudes at the peak and the
521 end of illumination were calculated using DataControl384 software v. 2.3.0 (Nanion Technologies). Further
522 analysis was performed using the Origin Pro 2016 software (OriginLab Corporation).

523 *Manual patch clamp recording using 1P excitation in HEK293 cells*

524 Manual patch clamp recordings were performed with an Axopatch 200B amplifier (Molecular Devices).
525 The pipette solution contained (in mM) KCl 130, MgCl2 2, HEPES 10 pH 7.4, and the bath solution contained
526 (in mM) NaCl 130, $CaCl_2$ 2, $MgCl_2$ 2, glucose 10, HEPES 10 pH 7.4. In experiments to test the relative
527 permeability of ChRs for Cl^-, NaCl in the bath was replaced with Na aspartate. The low-pass filter of the
528 amplifier output was set to 2 kHz. The signals were digitized with a Digidata 1440A (Molecular Devices) at
529 a 5 kHz sampling rate (200 µs per point) using pClamp 10.7. Patch pipettes with 2-3 MΩ resistances were
530 fabricated from borosilicate glass. Laser excitation was provided by a Minilite Nd:YAG laser (532 nm, pulse
531 width 6 ns, energy 5 mJ; Continuum). The current traces were logarithmically filtered using Logpro
532 software (Spudich, 2022). Curve fitting was performed using Origin Pro software. Continuous light pulses
533 were provided by a Polychrome V light source (T.I.L.L. Photonics GMBH) in combination with a mechanical
534 shutter (Uniblitz Model LS6, Vincent Associates; half-opening time 0.5 ms). The action spectra of
535 photocurrents were constructed by calculating the initial slope of photocurrent recorded in response to
536 15-ms light pulses at the intensity <25 µW mm^{-2}, corrected for the quantum density measured at each
537 wavelength, and normalized to the maximal value.

538 *Manual patch clamp recording using 2P excitation in HEK293A cells*

539 HEK293A cells were transfected using the pAAV-CAG-*Ans*ACR-EYFP plasmid. 2P excitation of *Ans*ACR was
540 conducted on an inverted microscope with multiphoton capability (A1R-MP, Nikon Instruments) at room
541 temperature. A coverslip seeded with the transfected cells was placed in a custom glass-bottom chamber
542 based on Chamlide EC (Live Cell Instrument) with a glass bottom made with a 24×24 mm cover glass #1
543 (Erie Scientific, Cat. #89082-270). Cells were perfused continuously with the external solution described
544 in the 1P excitation section. Whole-cell voltage-clamp recordings were performed using a MultiClamp
545 700B amplifier (Molecular Devices). The cells were held at −20 mV, with the command voltage
546 compensated for the 4.4 mV LJP calculated using the ClampEx v.11.1 (Molecular Devices) built-in
547 calculator. The signal was digitized with an Axon Digidata 1550B1 Low Noise system with HumSilencer
548 (Molecular Devices), and the current was recorded at 10 kHz using pClamp.

549 The near-IR excitation was generated by a titanium:sapphire femtosecond laser (Chameleon Ultra II,
550 Coherent) with a repetition rate of 80 MHz and a tuning range between 680 and 1,080 nm. Laser pulses
551 were not pre-compensated for dispersion in the microscope optical path. Laser power was tuned using an

552 acousto-optic modulator and delivered to the sample plane through a 40x0.95-numerical aperture (NA)
553 objective (CFI Plan Apochromat Lambda, Nikon Instruments). Scanning across xy regions-of-interest was
554 achieved using a resonant scanning microscope (Nikon A1RMP) at 33.3 Hz. An illumination "pulse"
555 consisted of 30 sequential raster scans (total duration ~1 s) over a 40.96×40.96 µm (512×512 pixels) area,
556 selected to approximate the average size of a HEK293A cell, and no time gap between each scan. To
557 determine the 2P action spectra of *Ans*ACR, the excitation wavelength was varied from 800 to 1,080 nm
558 in 40-nm increments. The laser was tuned to 7.5 mW at the sample plane at each wavelength measured
559 at the sample plane with a microscope slide power sensor (S170C, Thorlabs). This power level was chosen
560 to obtain robust photocurrents while remaining at or near the quadratic regime, where the slope of initial
561 photocurrents quadruples with a doubling of the excitation power. Deviations from the target power level
562 of 7.5 mW (<10%) were corrected by considering the quadratic dependence of photocurrents on power
563 under 2P excitation. To mitigate desensitization, we spaced illumination pulses ~55 s apart. We verified
564 that the power ramp and spectral scan protocols caused <20% reduction of the peak photocurrent,
565 measured during 7.5-mW, 920-nm light pulses applied at the start and end of each protocol. The 2P action
566 spectrum was constructed by measuring the initial linear slope of the photocurrent rise at each
567 wavelength and plotted using Origin Pro 2016 software (OriginLab Corporation).

568 *Expression and purification of ancyromonad ACRs from Pichia pastoris*

569 The plasmids carrying the expression constructs were linearized with Sac I and delivered into the *P. pastoris*
570 strain SMD1168 by electroporation. A single colony resistant to 0.25 mg/ml zeocin was picked and
571 inoculated into buffered complex glycerol medium, after which the cells were transferred to buffered
572 complex methanol (0.5%) medium supplemented with 5 µM all-*trans*-retinal (Millipore-Sigma, Cat. # 116-
573 31-4) and grown at 30 °C with shaking at 230 rpm. After 24 h, the yellow-colored cells were harvested by
574 centrifugation at 5000 g for 10 min, and the cell pellets were resuspended in 100 ml ice-cold buffer A
575 (20 mM HEPES, pH 7.4, 150 mM NaCl, 1 mM EDTA, 5% glycerol) and lysed by either French press or bead
576 beater. After centrifugation at low speed (5000 g for 10 min) to remove cell debris, membrane fractions
577 were pelleted at 190,000 g for 1 h using a Ti45 Beckman rotor. The membranes were suspended in Buffer
578 B (350 mM NaCl, 5% glycerol, 20 mM HEPES, pH 7.5) with 1 mM phenylmethylsulfonyl fluoride and
579 solubilized with 1% n-dodecyl-β-D-maltoside (DDM; Anatrace, Cat. # D310) for 1 h at 4 °C with shaking.
580 Undissolved content was removed after ultracentrifugation using a Ti45 rotor at 110,000 g for 1 h. The
581 supernatant supplemented with 15 mM imidazole was incubated with nickel-nitrilotriacetic acid resin
582 (Qiagen, Cat. # 30210) for 1 h with shaking at 4 °C. The resin was washed step-wise using 15 mM and
583 40 mM imidazole in Buffer B supplemented with 0.03% DDM. The protein was eluted with 400 mM
584 imidazole and 0.03% DDM in buffer B. Protein fractions were pooled and concentrated using a 50 kDa
585 MWCO Amicon Ultra Centrifugal Filter (Millipore-Sigma, Cat. # UFC9050), flash-frozen in liquid nitrogen
586 and stored at −80 °C until use.

587 *Absorption spectroscopy and flash photolysis*

588 Absorption spectra of detergent-purified protein samples were recorded using a Cary 4000
589 spectrophotometer (Varian). Photoinduced absorption changes were measured with a laboratory-
590 constructed crossbeam apparatus. Excitation flashes were provided by a Minilite II Nd:YAG laser (532 nm,
591 pulse width 6 ns, energy 5 mJ; Continuum). Measuring light was from a 250-W incandescent tungsten
592 lamp and a McPherson monochromator (model 272, Acton). Absorption changes were detected with a
593 Hamamatsu Photonics photomultiplier tube (model R928) combined with a second monochromator of

594 the same type. Signals were amplified by a low noise current amplifier (model SR445A; Stanford Research
595 Systems) and digitized with a GaGe Octopus digitizer board (model CS8327, DynamicSignals LLC), with a
596 maximal sampling rate of 50 MHz. Logarithmic data filtration was performed using the GageCon program
597 (Sineshchekov, Govorunova, Li, Wang, & Spudich, 2023).

598 *Mice*

599 All procedures to maintain and use mice were approved by the Institutional Animal Care and Use
600 Committee at Baylor College of Medicine (protocol AN-6544). Mice were maintained on a 14 hr:10 hr
601 light:dark cycle with regular mouse chow and water ad libitum. The temperature was maintained at 21–
602 25°C and humidity at 40-60%. Experiments were performed during the light cycle. Female ICR (CD-1) mice
603 were purchased from Baylor College of Medicine Center for Comparative Medicine, and male C57BL6/J
604 (JAX #000664) mice were obtained from Jackson Laboratory. Both male and female mice were used in the
605 experiments.

606 *In utero electroporation*

607 Female ICR mice were crossed with male C57BL6/J mice to obtain timed pregnancies. *In utero*
608 electroporation was used to deliver the transgenes (Xue, Atallah, & Scanziani, 2014). To express *Ans*ACR
609 or *Ft*ACR in the layer 2/3 pyramidal neurons of the somatosensory cortex, pAAV-CAG-*Ans*ACR-EYFP or
610 pAAV-CAG-*Ft*ACR-EYFP (2.5 µg $µl^{-1}$ final concentration) was mixed with pCAG-tdTomato (0.1 µg $µl^{-1}$ final
611 concentration) and Fast Green (Sigma-Aldrich, 0.01% final concentration) for injection. On embryonic day
612 15, pregnant mice were anesthetized, and a beveled glass micropipette (tip size 100-µm outer diameter,
613 50-µm inner diameter) was used to penetrate the uterus and the embryo skull to inject ~1.5 µl DNA
614 solution into one lateral ventricle. Five pulses of current (voltage 39 V, duration 50 ms) were delivered at
615 1 Hz with a Tweezertrode (5-mm diameter) and a square-wave pulse generator (Gemini X2, BTX Harvard
616 Bioscience). The electrode paddles were positioned in parallel with the brain's sagittal plane. The cathode
617 contacted the side of the brain ipsilateral to the injected ventricle to target the somatosensory cortex.
618 Transfected pups were identified by the transcranial fluorescence of tdTomato with an MZ10F
619 stereomicroscope (Leica) 1 day after birth.

620 *Brain slice electrophysiology and imaging*

621 Mice were used at the age of 4-6 weeks for acute brain slice electrophysiology experiments. Mice were
622 anesthetized by an intraperitoneal injection of a ketamine and xylazine mix (80 mg kg^{-1} and 16 mg kg^{-1},
623 respectively) and perfused transcardially with cold (0-4°C) slice cutting solution containing 80 mM NaCl,
624 2.5 mM KCl, 1.3 mM NaH_2PO_4, 26 mM $NaHCO_3$, 4 mM $MgCl_2$, 0.5 mM $CaCl_2$, 20 mM *d*-glucose, 75 mM
625 sucrose and 0.5 mM sodium ascorbate (315 mOsm l^{-1}, pH 7.4, saturated with 95% O_2/5% CO_2). Brains were
626 removed and sectioned in the cutting solution with a VT1200S vibratome (Leica) to obtain 300 µm coronal
627 slices. Slices were incubated in a custom-made interface holding chamber containing slice cutting solution
628 saturated with 95% O_2/5% CO_2 at 34°C for 30 min and then at room temperature for 20 min to 10 h until
629 they were transferred to the recording chamber. We performed recordings on submerged slices in artificial
630 cerebrospinal fluid (ACSF) containing 119 mM NaCl, 2.5 mM KCl, 1.3 mM NaH_2PO_4, 26 mM $NaHCO_3$, 1.3
631 mM $MgCl_2$, 2.5 mM $CaCl_2$, 20 mM *d*-glucose and 0.5 mM sodium ascorbate (305 mOsm l^{-1}, pH 7.4,
632 saturated with 95% O_2/5% CO_2, perfused at 3 ml min^{-1}) at 30-32°C. For whole-cell recordings, a K^+-based
633 pipette solution containing 142 mM K^+ gluconate, 10 mM HEPES, 1 mM EGTA, 2.5 mM $MgCl_2$, 4 mM ATP-
634 Mg, 0.3 mM GTP-Na, 10 mM Na_2-phosphocreatine (295 mOsm l^{-1}, pH 7.35) was used. Membrane

potentials reported in Figure 6 and Figure 6 – figure supplement 1 were not corrected for LJP, which was 12.5 mV as measured experimentally. Neurons were visualized with video-assisted IR differential interference contrast imaging, and fluorescent neurons were identified by epifluorescence imaging under a water immersion objective (×40, 0.8 NA) on an upright SliceScope Pro 1000 microscope (Scientifica) with an IR-1000 CCD camera (DAGE-MTI). Data were acquired at 10 kHz and low-pass filtered at 4 kHz with an Axon Multiclamp 700B amplifier and an Axon Digidata 1440 A Data Acquisition System under the control of Clampex 10.7 (Molecular Devices). Data were analyzed offline using Clampfit (Molecular Devices). For photostimulation, blue light was emitted from a collimated 470 nm light-emitting diode (LED; M470L3, Thorlabs) to stimulate *Ans*ACR- or *Ft*ACR-expressing neurons. The LEDs were driven by a LED driver (Throlabs LEDD1B) under the control of an Axon Digidata 1440 A Data Acquisition System and Clampex 10.7. The light was delivered through the reflected light fluorescence illuminator port and the ×40 objective.

To evaluate inhibition efficiency, action potentials of *Ans*ACR- or *Ft*ACR-expressing neurons were evoked by injecting a series of 1.5-s depolarizing current pulses (-0.1-0.5 nA) in whole-cell current clamp mode. 1-s 470 nm (38.7 mW mm^{-2}) light stimulation was applied in the middle of current injections with 30-s inter-trial-interval. Resting membrane potentials, input resistances, and capacitances were measured in the trials with -0.1 nA current injection. To examine the excitatory effect of the ACRs, 10-ms 470 nm (38.7 mW mm^{-2}) light stimulation was applied, and ACR^- neurons were clamped at -70 mV to record excitatory post-synaptic currents. Only recordings with R_a < 20 MΩ were included in the analysis.

After electrophysiology recordings, fluorescent images of the brain slices were acquired on an Axio Zoom.V16 Fluorescence Stereo Zoom Microscope (Zeiss) and processed using MATLAB2024b (MathWorks). Images were taken from 20 brain slices of two male and two female mice.

Generation of transgenic C. elegans strains and EPG recording

The transgenic *C. elegans* strains COP2831 and COP2832 [*uncp*-17::*Ans*ACR::EYFP::*tbb-2u*], *unc-119*(+))} II; *unc-119(ed3)* III expressing *Ans*ACR in cholinergic neurons were created by InVivo Biosystems using the Mos1-mediated Single Copy Insertion (MosSCI) method, which enables integrating the transgene as a single-copy insertion at a designated locus in the *C. elegans* genome (Frokjaer-Jensen, 2015). *Unc*-119 rescue cassette insertion was used to bring the transgene into a Mos1 target locus on chromosome II and create rescue of the function of the *unc-119(ed3)* III mutant allele. The Mos1 locus was selected for position-neutral effects and to avoid the gene coding regions, introns, and transcription factor binding sites. The integration of the transgene was confirmed by PCR.

The transgenic and Bristol N2 wild-type worms were grown at 20°C on *E. coli* strain OP50 lawns in the absence or presence of 10 µM (final concentration) all-*trans*-retinal (Millipore-Sigma, Cat. # 116-31-4), which was mixed with the bacteria before seeding Nematode Growth Medium (NGM) plates. EPG recordings were performed from intact worms sucked into a pipette (Raizen & Avery, 1994). The pipettes (200 kΩ resistance) were pulled from borosilicate glass and filled with the External Physiological solution, the composition of which is specified in the above section. The worms were transferred to the same solution supplemented with 10 mM serotonin before the measurements. The data were acquired in the voltage clamp mode of the same Axopatch 200B amplifier used for manual patch clamp recording from HEK293 cells and the same software. The data obtained in two independently created strains were pooled together. The photoexcitation was provided by the Polychrome V light source described above. The frequency of the R1-spikes was calculated using the Event Detection by the Threshold Search function of

677 ClampFit after applying a 2-Hz high-pass digital filter. Further analysis was performed using the Origin Pro
678 2016 software.

679 *Reproducibility and statistics*

680 Plasmids encoding different ChR variants were randomly assigned to transfect identical cell batches. Three
681 independent transfections were performed on different experimental days; the data obtained were pooled
682 together. In automated patch clamp studies, cells were randomly drawn into the wells. For an unbiased
683 estimation of the photocurrent amplitude, the data from wells that formed seals with a resistance <500
684 MΩ were excluded. For a more accurate estimation of the V_r values by plotting the IV curves, wells with a
685 seal resistance <500 MΩ and photocurrents of the absolute magnitude <50 pA at -80 mV were excluded.
686 In manual patch clamp experiments, the cells were selected for patching by inspecting their tag
687 fluorescence; non-fluorescent cells and cells in which no GΩ seal was established or lost during recording
688 were excluded from the analysis. In automated and manual patch clamp experiments, the photocurrent
689 traces recorded from different cells transfected with the same construct were considered biological
690 replicates (reported as n values). These values indicate how often the experiments were performed
691 independently.

692 Statistical analysis of the patch clamp data was performed using Origin Pro 2016 software. The normal
693 distribution of the data was not assumed. The non-parametric two-tailed Mann-Whitney and Kolmogorov-
694 Smirnov tests were used to compare the means. No statistical methods were used to pre-determine
695 sample sizes, but the sample sizes were similar to those reported in the previous publications
696 (Govorunova, Gou, et al., 2022; Morizumi et al., 2023). }. Statistical analysis of the cortical neuron patch
697 clamp data was performed using ClampFit 10.7 (Molecular Devices) and Prism 10.3 (GraphPad).

698 *Data availability*

699 The numerical data and statistical analyses are provided in the Suppl. Data File 1. The sequence
700 information was deposited at the NCBI with GenBank accession numbers PQ657777-PQ657783. The
701 plasmids encoding *Ans*ACR, *Ft*ACR, and *Nl*CCR expression constructs in the pcDNA3.1 vector backbone
702 were deposited at Addgene (plasmids #232598, 232599, and 232600, respectively). The plasmids pAAV-
703 CAG-*Ans*ACR-EYFP and pAAV-CAG-*Ft*ACR-EYFP were deposited at Addgene (plasmids #XXX and #YYY,
704 respectively).

705 *Acknowledgments*

706 We thank Dr. Valeria Vasquez (UTHealth) for a generous donation of the wild-type *C. elegans* strain and
707 OP50 *E. coli* strain. This work was supported by the National Institutes of Health Grants R35GM140838
708 (J.L.S.), S10OD032293-01 (J.L.S.), and U01NS118288 (M.X., J.L.S., F.S.P.); the Robert A. Welch Foundation
709 Endowed Chair AU-0009 (J.L.S.); a Vivian L. Smith Endowed Professorship in Neuroscience (F.S.P); the
710 McNair Medical Foundation (F.S.P); and NIH grant R61CA278458 (F.S.P.); the Natural Sciences and
711 Engineering Research Council of Canada (NSERC) grants RGPIN-2018-04397 and RGPIN-2024-03857
712 (L.S.B.). An NSERC USRA award supported A.P., and S.M. was supported by the President's Research
713 Assistantship (PRA) program at the University of Guelph. M.X. is a Caroline DeLuca Scholar.

714 *Declaration of interests*

M.X. was a consultant to Capsida Biotherapeutics. Capsida Biotherapeutics provided research funds to Baylor College of Medicine to support a research project in his lab that is unrelated to this study and had no role in the research, authorship, and publication of this article.

References

Alam, I., Kamau, A. A., Ngugi, D. K., Gojobori, T., Duarte, C. M., & Bajic, V. B. (2021). KAUST Metagenomic Analysis Platform (KMAP), enabling access to massive analytics of re-annotated metagenomic data. *Sci Rep, 11*(1), 11511. doi:10.1038/s41598-021-90799-y

Amses, K. R., Simmons, D. R., Longcore, J. E., Mondo, S. J., Seto, K., Jeronimo, G. H., . . . James, T. Y. (2022). Diploid-dominant life cycles characterize the early evolution of Fungi. *Proc Natl Acad Sci U S A, 119*(36), e2116841119. doi:10.1073/pnas.2116841119

Bergs, A., Henss, T., Glock, C., Nagpal, J., & Gottschalk, A. (2022). Microbial rhodopsin optogenetic tools: Application for analyses of synaptic transmission and of neuronal network activity in behavior. *Methods Mol Biol, 2468*, 89-115. doi:10.1007/978-1-0716-2181-3_6

Bhatla, N., & Horvitz, H. R. (2015). Light and hydrogen peroxide inhibit *C. elegans* feeding through gustatory receptor orthologs and pharyngeal neurons. *Neuron, 85*(4), 804-818. doi:10.1016/j.neuron.2014.12.061

Brown, M. W., Heiss, A. A., Kamikawa, R., Inagaki, Y., Yabuki, A., Tice, A. K., . . . Roger, A. J. (2018). Phylogenomics places orphan protistan lineages in a novel eukaryotic super-group. *Genome Biol Evol, 10*(2), 427-433. doi:10.1093/gbe/evy014

Chen, F., Duan, X., Yu, Y., Yang, S., Chen, Y., Gee, C. E., . . . Shen, Y. (2022). Visual function restoration with a highly sensitive and fast channelrhodopsin in blind mice. *Signal Transduct. Target. Ther., 7*(1), 104. doi:10.1038/s41392-022-00935-x

Deisseroth, K. (2021). From microbial membrane proteins to the mysteries of emotion. *Cell*. doi:10.1016/j.cell.2021.08.018

Emiliani, V., Entcheva, E., Hedrich, R., Hegemann, P., Konrad, K. R., Lüscher, C., . . . Yizhar, O. (2022). Optogenetics for light control of biological systems. *Nature Reviews Methods Primers, 2*(1), 55. doi:10.1038/s43586-022-00136-4

Engqvist, M. K., McIsaac, R. S., Dollinger, P., Flytzanis, N. C., Abrams, M., Schor, S., & Arnold, F. H. (2015). Directed evolution of *Gloeobacter violaceus* rhodopsin spectral properties. *J. Mol. Biol., 427*, 205-220. doi:10.1016/j.jmb.2014.06.015

Ernst, O. P., Lodowski, D. T., Elstner, M., Hegemann, P., Brown, L. S., & Kandori, H. (2014). Microbial and animal rhodopsins: structures, functions, and molecular mechanisms. *Chem. Rev., 114*(1), 126-163. doi:10.1021/cr4003769

Frokjaer-Jensen, C. (2015). Transposon-assisted genetic engineering with Mos1-mediated single-copy insertion (MosSCI). *Methods Mol Biol, 1327*, 49-58. doi:10.1007/978-1-4939-2842-2_5

Govorunova, E. G., Gou, Y., Sineshchekov, O. A., Li, H., Lu, X., Wang, Y., . . . Spudich, J. L. (2022). Kalium channelrhodopsins are natural light-gated potassium channels that mediate optogenetic inhibition. *Nat. Neurosci., 25*(7), 967-974. doi:10.1038/s41593-022-01094-6

Govorunova, E. G., Jung, K.-W., Sineshchekov, O. A., & Spudich, J. L. (2004). *Chlamydomonas* sensory rhodopsins A and B: Cellular content and role in photophobic responses. *Biophys. J., 86*, 2342-2349. doi:10.1016/S0006-3495(04)74291-5

Govorunova, E. G., Sineshchekov, O. A., Brown, L. S., & Spudich, J. L. (2022). Biophysical characterization of light-gated ion channels using planar automated patch clamp. *Front. Mol. Neurosci., 15*, 976910. doi:10.3389/fnmol.2022.976910

Govorunova, E. G., Sineshchekov, O. A., Li, H., Janz, R., & Spudich, J. L. (2013). Characterization of a highly efficient blue-shifted channelrhodopsin from the marine alga *Platymonas subcordiformis*. *J. Biol. Chem., 288*(41), 29911-29922. doi:10.1074/jbc.M113.505495

Govorunova, E. G., Sineshchekov, O. A., Li, H., Wang, Y., Brown, L. S., Palmateer, A., . . . Spudich, J. L. (2021). Cation and anion channelrhodopsins: Sequence motifs and taxonomic distribution. *MBio, 12*, e0165621. doi:10.1128/mBio.01656-21

Govorunova, E. G., Sineshchekov, O. A., Li, H., Wang, Y., Brown, L. S., & Spudich, J. L. (2020). RubyACRs, non-algal anion channelrhodopsins with highly red-shifted absorption. *Proc. Natl. Acad. Sci. USA, 117*, 22833-22840. doi:10.1073/pnas.2005981117

Govorunova, E. G., Sineshchekov, O. A., Liu, X., Janz, R., & Spudich, J. L. (2015). Natural light-gated anion channels: A family of microbial rhodopsins for advanced optogenetics. *Science, 349*(6248), 647-650. doi:10.1126/science.aaa7484

Govorunova, E. G., Sineshchekov, O. A., & Spudich, J. L. (2022). Emerging diversity of channelrhodopsins and their structure-function relationships. *Front Cell Neurosci, 15*, 800313. doi:10.3389/fncel.2021.800313

Govorunova, E. G., Sineshchekov, O. A., & Spudich, J. L. (2023). Potassium-selective channelrhodopsins. *Biophysics and Physicobiology, 20*, e201011. doi:10.2142/biophysico.bppb-v20.s011

Grigoriev, I. V., Nikitin, R., Haridas, S., Kuo, A., Ohm, R., Otillar, R., . . . Shabalov, I. (2014). MycoCosm portal: gearing up for 1000 fungal genomes. *Nucleic Acids Res, 42*(Database issue), D699-704. doi:10.1093/nar/gkt1183

Hoang, D. T., Chernomor, O., von Haeseler, A., Minh, B. Q., & Vinh, L. S. (2018). UFBoot2: Improving the ultrafast bootstrap approximation. *Mol. Biol. Evol., 35*(2), 518-522. doi:10.1093/molbev/msx281

Hochbaum, D. R., Zhao, Y., Farhi, S. L., Klapoetke, N., Werley, C. A., Kapoor, V., . . . Cohen, A. E. (2014). All-optical electrophysiology in mammalian neurons using engineered microbial rhodopsins. *Nat. Methods, 8*, 825-833. doi:10.1038/nmeth.3000

Hoffmann, M., Wanko, M., Strodel, P., Konig, P. H., Frauenheim, T., Schulten, K., . . . Elstner, M. (2006). Color tuning in rhodopsins: the mechanism for the spectral shift between bacteriorhodopsin and sensory rhodopsin II. *J. Am. Chem. Soc., 128*(33), 10808-10818. doi:10.1021/ja062082i

Inoue, K., Del Carmen Marin, M., Tomida, S., Nakamura, R., Nakajima, Y., Olivucci, M., & Kandori, H. (2019). Red-shifting mutation of light-driven sodium-pump rhodopsin. *Nat. Commun., 10*(1), 1993. doi:10.1038/s41467-019-10000-x

Janouškovec, J., Tikhonenkov, D. V., Burki, F., Howe, A. T., Rohwer, F. L., Mylnikov, A. P., & Keeling, P. J. (2017). A new lineage of eukaryotes illuminates early mitochondrial genome reduction. *Curr Biol, 27*(23), 3717-3724 e3715. doi:10.1016/j.cub.2017.10.051

Karasuyama, M., Inoue, K., Nakamura, R., Kandori, H., & Takeuchi, I. (2018). Understanding colour tuning rules and predicting absorption wavelengths of microbial rhodopsins by data-driven machine-learning approach. *Sci. Rep., 8*(1), 15580. doi:10.1038/s41598-018-33984-w

Kato, H. E., Kamiya, M., Sugo, S., Ito, J., Taniguchi, R., Orito, A., . . . Nureki, O. (2015). Atomistic design of microbial opsin-based blue-shifted optogenetics tools. *Nat. Commun., 6*, 7177. doi:10.1038/ncomms8177

Kim, Y. S., Kato, H. E., Yamashita, K., Ito, S., Inoue, K., Ramakrishnan, C., . . . Deisseroth, K. (2018). Crystal structure of the natural anion-conducting channelrhodopsin *Gt*ACR1. *Nature, 561*, 343-348. doi:10.1038/s41586-018-0511-6

Letunic, I., & Bork, P. (2024). Interactive Tree of Life (iTOL) v6: recent updates to the phylogenetic tree display and annotation tool. *Nucleic Acids Res, 52*(W1), W78-W82. doi:10.1093/nar/gkae268

Li, H., Huang, C. Y., Govorunova, E. G., Schafer, C. T., Sineshchekov, O. A., Wang, M., . . . Spudich, J. L. (2019). Crystal structure of a natural light-gated anion channelrhodopsin. *Elife, 8*, e41741. doi:10.7554/eLife.41741

Mahn, M., Gibor, L., Patil, P., Cohen-Kashi Malina, K., Oring, S., Printz, Y., . . . Yizhar, O. (2018). High-efficiency optogenetic silencing with soma-targeted anion-conducting channelrhodopsins. *Nat. Commun., 9*(1), 4125. doi:10.1038/s41467-018-06511-8

Man, D., Wang, W., Sabehi, G., Aravind, L., Post, A. F., Massana, R., . . . Béjà, O. (2003). Diversification and spectral tuning in marine proteorhodopsins. *EMBO J., 22*, 1725-1731.

Messier, J. E., Chen, H., Cai, Z. L., & Xue, M. (2018). Targeting light-gated chloride channels to neuronal somatodendritic domain reduces their excitatory effect in the axon. *Elife, 7*, e38506. doi:10.7554/eLife.38506

Minh, B. Q., Schmidt, H. A., Chernomor, O., Schrempf, D., Woodhams, M. D., von Haeseler, A., & Lanfear, R. (2020). IQ-TREE 2: New models and efficient methods for phylogenetic inference in the genomic era. *Mol. Biol. Evol., 37*(5), 1530-1534. doi:10.1093/molbev/msaa015

Morizumi, T., Kim, K., Li, H., Govorunova, E. G., Sineshchekov, O. A., Wang, Y., . . . Ernst, O. P. (2023). Structures of channelrhodopsin paralogs in peptidiscs explain their contrasting K^+ and Na^+ selectivities. *Nat Commun, 14*(1), 4365. doi:10.1038/s41467-023-40041-2

Nanjappa, D., Sanges, R., Ferrante, M. I., & Zingone, A. (2017). Diatom flagellar genes and their expression during sexual reproduction in *Leptocylindrus danicus*. *BMC Genomics, 18*(1), 813. doi:10.1186/s12864-017-4210-8

Oda, K., Vierock, J., Oishi, S., Rodriguez-Rozada, S., Taniguchi, R., Yamashita, K., . . . Nureki, O. (2018). Crystal structure of the red light-activated channelrhodopsin Chrimson. *Nat. Commun., 9*, 3949. doi:10.1038/s41467-018-06421-9

Oppermann, J., Rozenberg, A., Fabrin, T., Gonzalez-Cabrera, C., Parker, R., Beja, O., . . . Hegemann, P. (2024). Robust optogenetic inhibition with red-light-sensitive anion-conducting channelrhodopsins. *Elife, 12*. doi:10.7554/eLife.90100

Piatkevich, K. D., & Boyden, E. S. (2023). Optogenetic control of neural activity: the Biophysics of microbial rhodopsins in neuroscience. *Q Rev Biophys*, 1-81. doi:10.1017/S0033583523000033

Priyam, A., Woodcroft, B. J., Rai, V., Moghul, I., Munagala, A., Ter, F., . . . Wurm, Y. (2019). Sequenceserver: A modern graphical user interface for custom BLAST databases. *Mol Biol Evol, 36*(12), 2922-2924. doi:10.1093/molbev/msz185

Raizen, D. M., & Avery, L. (1994). Electrical activity and behavior in the pharynx of *Caenorhabditis elegans*. *Neuron, 12*(3), 483-495. doi:10.1016/0896-6273(94)90207-0

Richter, D. J., Berney, C., Strassert, J. F. H., Poh, Y.-P., Herman, E. K., Muñoz-Gómez, S. A., . . . de Vargas, C. (2022). EukProt: A database of genome-scale predicted proteins across the diversity of eukaryotes. *Peer Community Journal, 2*, e56. doi:10.24072/pcjournal.173

Rozenberg, A. (2024). *A catalog of natural channelrhodopsins*.

Rozenberg, A., Oppermann, J., Wietek, J., Fernandez Lahore, R. G., Sandaa, R. A., Bratbak, G., . . . Béjà, O. (2020). Lateral gene transfer of anion-conducting channelrhodopsins between green algae and giant viruses. *Curr. Biol., 30*, 4910-4920. doi:10.1016/j.cub.2020.09.056

Sakamoto, M., & Yokoyama, T. (2024). Probing neuronal activity with genetically encoded calcium and voltage fluorescent indicators. *Neurosci Res*. doi:10.1016/j.neures.2024.06.004

Schüler, C., Fischer, E., Shaltiel, L., Steuer Costa, W., & Gottschalk, A. (2015). Arrhythmogenic effects of mutated L-type Ca^{2+}-channels on an optogenetically paced muscular pump in *Caenorhabditis elegans*. *Sci Rep, 5*, 14427. doi:10.1038/srep14427

Shimono, K., Iwamoto, M., Sumi, M., & Kamo, N. (2000). Effects of three characteristic amino acid residues of pharaonis phoborhodopsin on the absorption maximum. *Photochem. Photobiol., 72*, 141-145.

Shimono, K., Kitami, M., Iwamoto, M., & Kamo, N. (2000). Involvement of two groups in reversal of the bathochromic shift of pharaonis phoborhodopsin by chloride at low pH. *Biophys. Chem., 87*(2-3), 225-230.

Sineshchekov, O. A., Govorunova, E. G., Li, H., & Spudich, J. L. (2015). Gating mechanisms of a natural anion channelrhodopsin. *Proc. Natl. Acad. Sci. USA, 112*, 14236-14241. doi:10.1073/pnas.1513602112

Sineshchekov, O. A., Govorunova, E. G., Li, H., Wang, Y., & Spudich, J. L. (2023). Sequential absorption of two photons creates a bistable form of RubyACR responsible for its strong desensitization. *Proc Natl Acad Sci U S A, 120*(21), e2301521120. doi:10.1073/pnas.2301521120

Sineshchekov, O. A., Jung, K.-H., & Spudich, J. L. (2002). Two rhodopsins mediate phototaxis to low- and high-intensity light in *Chlamydomonas reinhardtii*. *Proc. Natl. Acad. Sci. USA, 99*, 8689-8694. doi:10.1073/pnas.122243399

Sineshchekov, O. A., Li, H., Govorunova, E. G., & Spudich, J. L. (2016). Photochemical reaction cycle transitions during anion channelrhodopsin gating. *Proc. Natl. Acad. Sci. USA, 113*, E1993-2000. doi:10.1073/pnas.1525269113

Spudich, E. N., Ozorowski, G., Schow, E. V., Tobias, D. J., Spudich, J. L., & Luecke, H. (2012). A transporter converted into a sensor, a phototaxis signaling mutant of bacteriorhodopsin at 3.0 A. *J. Mol. Biol., 415*(3), 455-463. doi:10.1016/j.jmb.2011.11.025

Spudich, J. L. (2022). LogPro: Zenodo. Retrieved from https://doi.org/10.5281/zenodo.6461999

Sudo, Y., Okazaki, A., Ono, H., Yagasaki, J., Sugo, S., Kamiya, M., . . . Hayashi, S. (2013). A blue-shifted light-driven proton pump for neural silencing. *J. Biol. Chem., 288*(28), 20624-20632. doi:10.1074/jbc.M113.475533

Sunagawa, S., Coelho, L. P., Chaffron, S., Kultima, J. R., Labadie, K., Salazar, G., . . . Bork, P. (2015). Ocean plankton. Structure and function of the global ocean microbiome. *Science, 348*(6237), 1261359. doi:10.1126/science.1261359

Tajima, S., Kim, Y. S., Fukuda, M., Jo, Y., Wang, P. Y., Paggi, J. M., . . . Kato, H. E. (2023). Structural basis for ion selectivity in potassium-selective channelrhodopsins. *Cell*. doi:10.1016/j.cell.2023.08.009

Tashiro, R., Sushmita, K., Hososhima, S., Sharma, S., Kateriya, S., Kandori, H., & Tsunoda, S. P. (2021). Specific residues in the cytoplasmic domain modulate photocurrent kinetics of channelrhodopsin from the alga *Klebsormidium nitens*. *Commun. Biol., 4*, 235. doi:10.1038/s42003-021-01755-5

Tikhonenkov, D. V., Mikhailov, K. V., Gawryluk, R. M. R., Belyaev, A. O., Mathur, V., Karpov, S. A., . . . Keeling, P. J. (2022). Microbial predators form a new supergroup of eukaryotes. *Nature, 612*(7941), 714-719. doi:10.1038/s41586-022-05511-5

Torruella, G., de Mendoza, A., Grau-Bove, X., Anto, M., Chaplin, M. A., del Campo, J., . . . Ruiz-Trillo, I. (2015). Phylogenomics reveals convergent evolution of lifestyles in close relatives of animals and fungi. *Curr Biol, 25*(18), 2404-2410. doi:10.1016/j.cub.2015.07.053

Trojanowski, N. F., Padovan-Merhar, O., Raizen, D. M., & Fang-Yen, C. (2014). Neural and genetic degeneracy underlies *Caenorhabditis elegans* feeding behavior. *J Neurophysiol, 112*(4), 951-961. doi:10.1152/jn.00150.2014

Trojanowski, N. F., Raizen, D. M., & Fang-Yen, C. (2016). Pharyngeal pumping in *Caenorhabditis elegans* depends on tonic and phasic signaling from the nervous system. *Sci Rep, 6*, 22940. doi:10.1038/srep22940

Tsujimura, M., Noji, T., Saito, K., Kojima, K., Sudo, Y., & Ishikita, H. (2021). Mechanism of absorption wavelength shifts in anion channelrhodopsin-1 mutants. *Biochim. Biophys. Acta Bioenerg., 1862*, 148349. doi:10.1016/j.bbabio.2020.148349

Tucker, K., Sridharan, S., Adesnik, H., & Brohawn, S. G. (2022). Cryo-EM structures of the channelrhodopsin ChRmine in lipid nanodiscs. *Nat Commun, 13*(1), 4842. doi:10.1038/s41467-022-32441-7

Varo, G., Brown, L. S., Needleman, R., & Lanyi, J. K. (1996). Proton transport by halorhodopsin. *Biochemistry, 35*(21), 6604-6611. doi:10.1021/bi9601159

Villar, E., Vannier, T., Vernette, C., Lescot, M., Cuenca, M., Alexandre, A., . . . Hingamp, P. (2018). The Ocean Gene Atlas: exploring the biogeography of plankton genes online. *Nucleic Acids Res., 46*(W1), W289-W295. doi:10.1093/nar/gky376

Volkov, O., Kovalev, K., Polovinkin, V., Borshchevskiy, V., Bamann, C., Astashkin, R., . . . Gordeliy, V. (2017). Structural insights into ion conduction by channelrhodopsin 2. *Science, 358*(6366), eaan8862. doi:10.1126/science.aan8862

Wang, Y. Z., Natsume, K., Tanaka, T., Hososhima, S., Tashiro, R., Sano, F. K., . . . Nureki, O. (2024). cryo-EM structure of a blue-shifted channelrhodopsin from *Klebsormidium nitens*. *BioRxiv*, 2024.2001.2021.576531. doi:10.1101/2024.01.21.576531

Xue, M., Atallah, B. V., & Scanziani, M. (2014). Equalizing excitation-inhibition ratios across visual cortical neurons. *Nature, 511*(7511), 596-600. doi:10.1038/nature13321

Zabelskii, D., Alekseev, A., Kovalev, K., Rankovic, V., Balandin, T., Soloviov, D., . . . Gordeliy, V. (2020). Viral rhodopsins 1 are an unique family of light-gated cation channels. *Nat. Commun., 11*(1), 5707. doi:10.1038/s41467-020-19457-7

Figure supplement and their legends

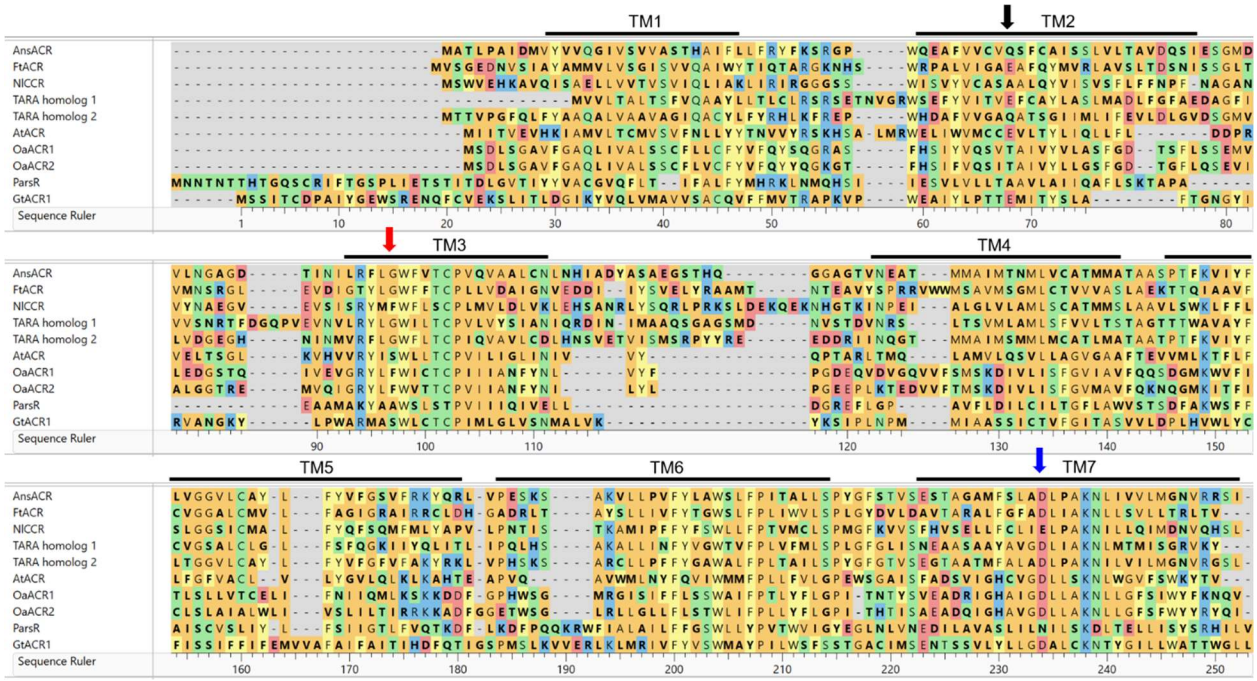

Figure 1 – figure supplement 1. The protein alignment of the 7TM domains of ChR variants identified and characterized in this study and the previously known *Gt*ACR1.

The amino acid residues are colored according to their chemical properties. The residue ruler is according to the *Gt*ACR1 sequence. The lines show the transmembrane helices TM1-TM7 of *Gt*ACR1. The arrows point to the positions corresponding to Asp68 (black), Ser97 (red), and Asp234 (blue) of *Gt*ACR1.

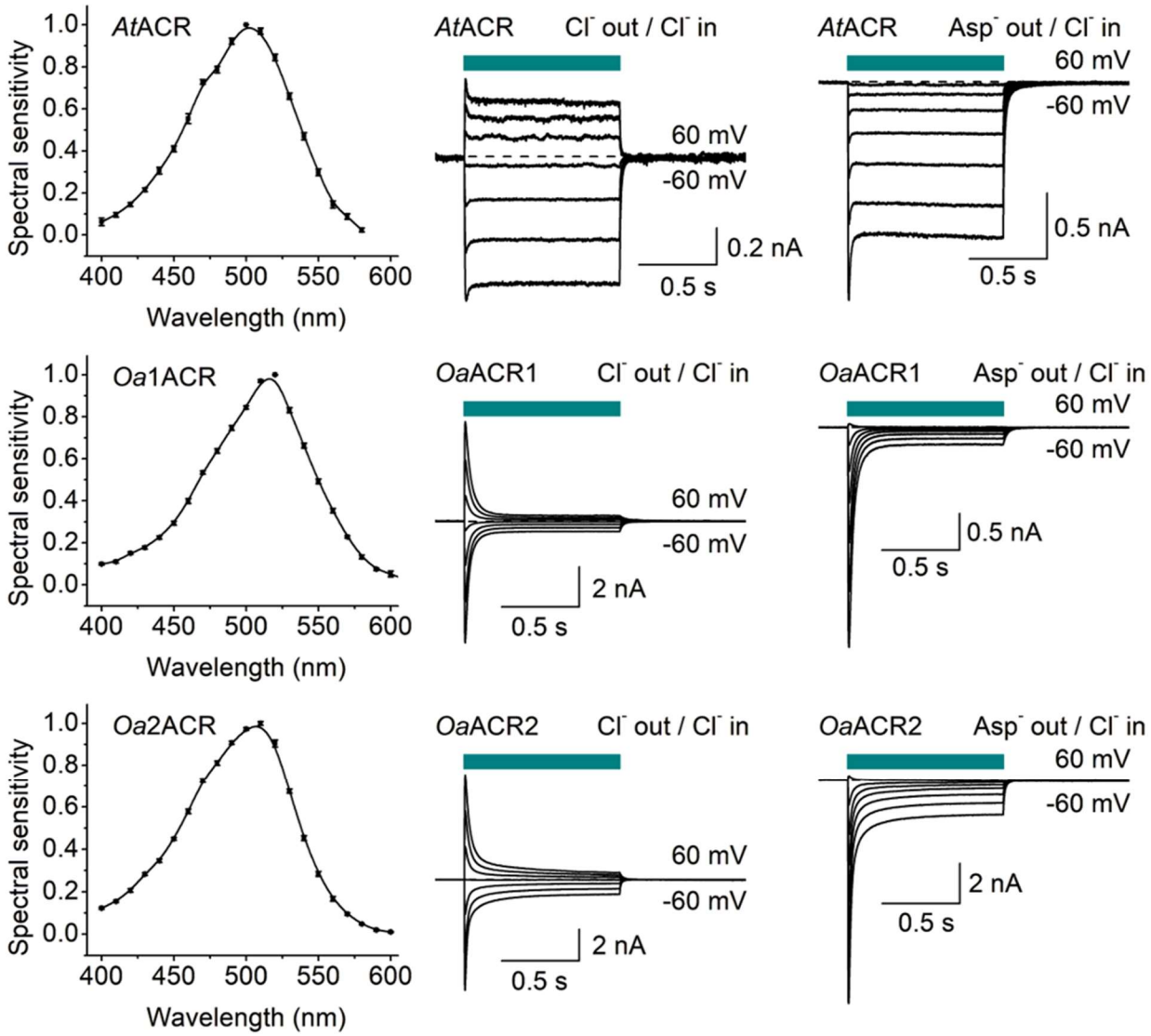

Figure 1 – figure supplement 2. Action spectra and photocurrents of ACRs from *Ancoracysta twista* and *Odontella aurita.*

In the left panels, the action spectra. The symbols are the mean values, and the error bars are SEM values; n = 6 cells for each variant. In the middle and right panels, the photocurrents recorded by manual patch clamping in the Cl^- bath (middle) and Asp^- bath (right) at the holding voltages increased in 20-mV increments from -60 mV. The dark cyan bars show the duration of illumination (500, 520 and 510 nm, respectively, for *At*ACR, *Oa*ACR1, and *Oa*ACR2).

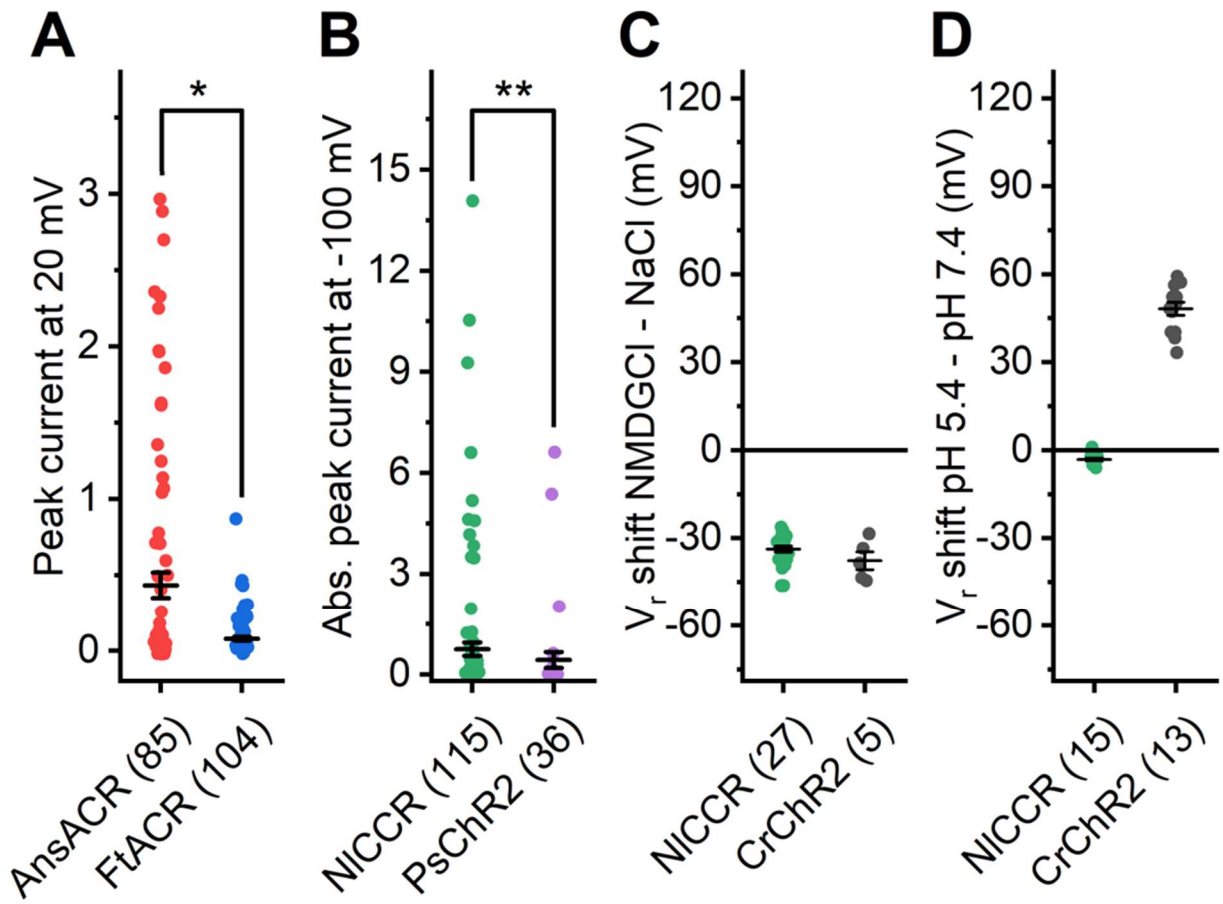

Figure 2 – figure supplement 1. Photocurrent amplitudes of anycromonad ChRs and comparison of *Nl*CCR with *Cr*ChR2.

(**A, B**) Unbiased estimation of peak photocurrent amplitudes. The photocurrents were recorded at 20 mV for *Ans*ACR and *Ft*ACR, and at -60 mV for *Nl*CCR and *Ps*ChR2. *, p = 0.0047; **, p = 9.9E10-6 by the two-tailed, two-sample Kolmogorov-Smirnov test. (**C, D**) The V_r shifts measured upon replacing Na^+ with $NMDG^+$ in the external solution (C), and upon its acidification from pH 7.4 to 5.4 (D). In all panels, the symbols are the data from individual cells; the lines are the mean and SEM values; the numbers in brackets are the numbers of cells sampled.

The online version of this article includes the following source data for Figure 2 – figure supplement 1:
Source data 1. Source data for the numbers of cells sampled and numerical values shown in (A-D).

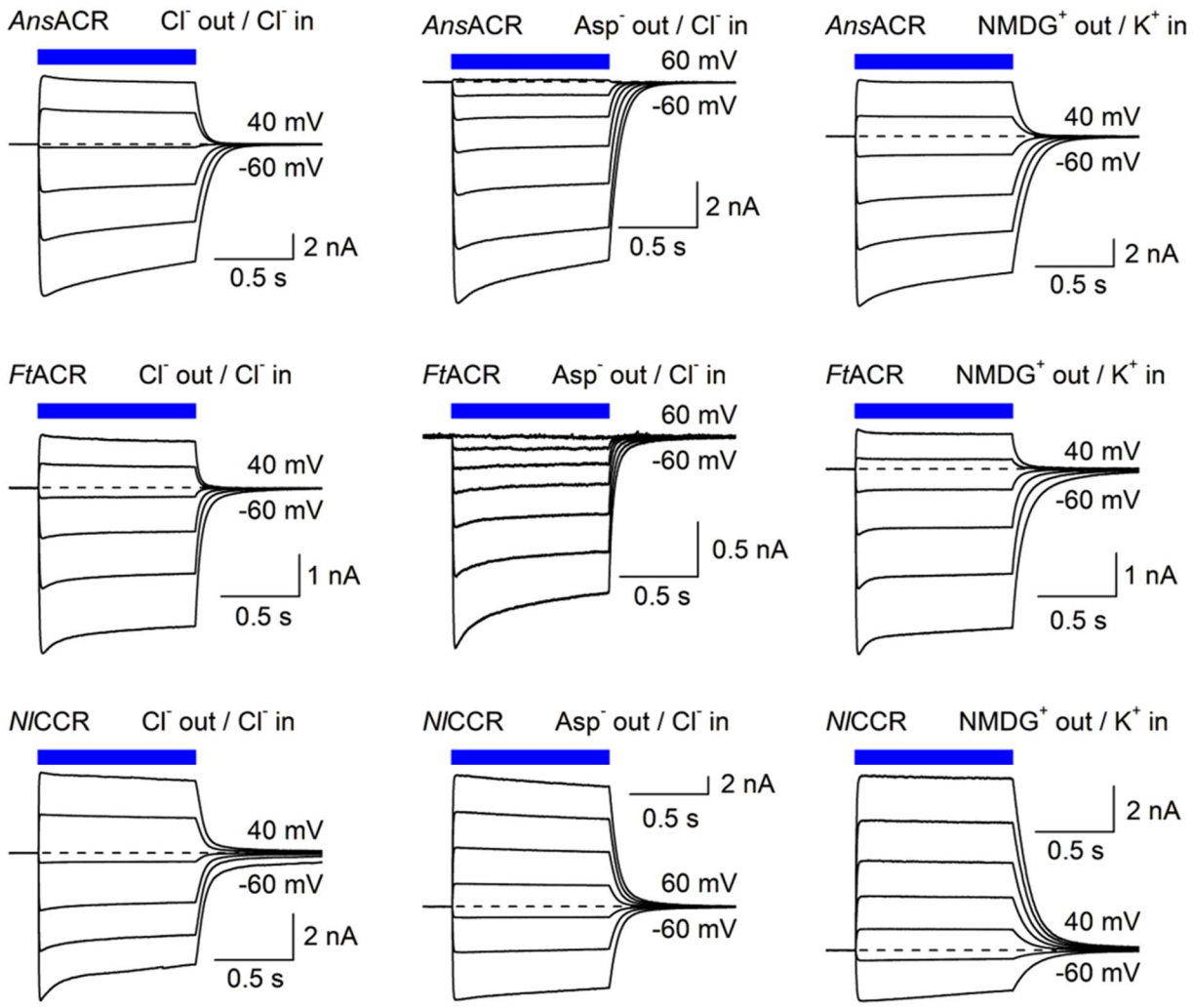

Figure 2 – figure supplement 2. Photocurrent traces recorded from ancyromonad ChRs by manual patch clamping.

The photocurrents were recorded by manual patch clamping in the Cl^- bath (left), Asp^- bath (middle), and $NMDG^+$ bath (right) at the holding voltages increased in 20-mV increments from -60 mV. The blue bars show the duration of 470 nm illumination.

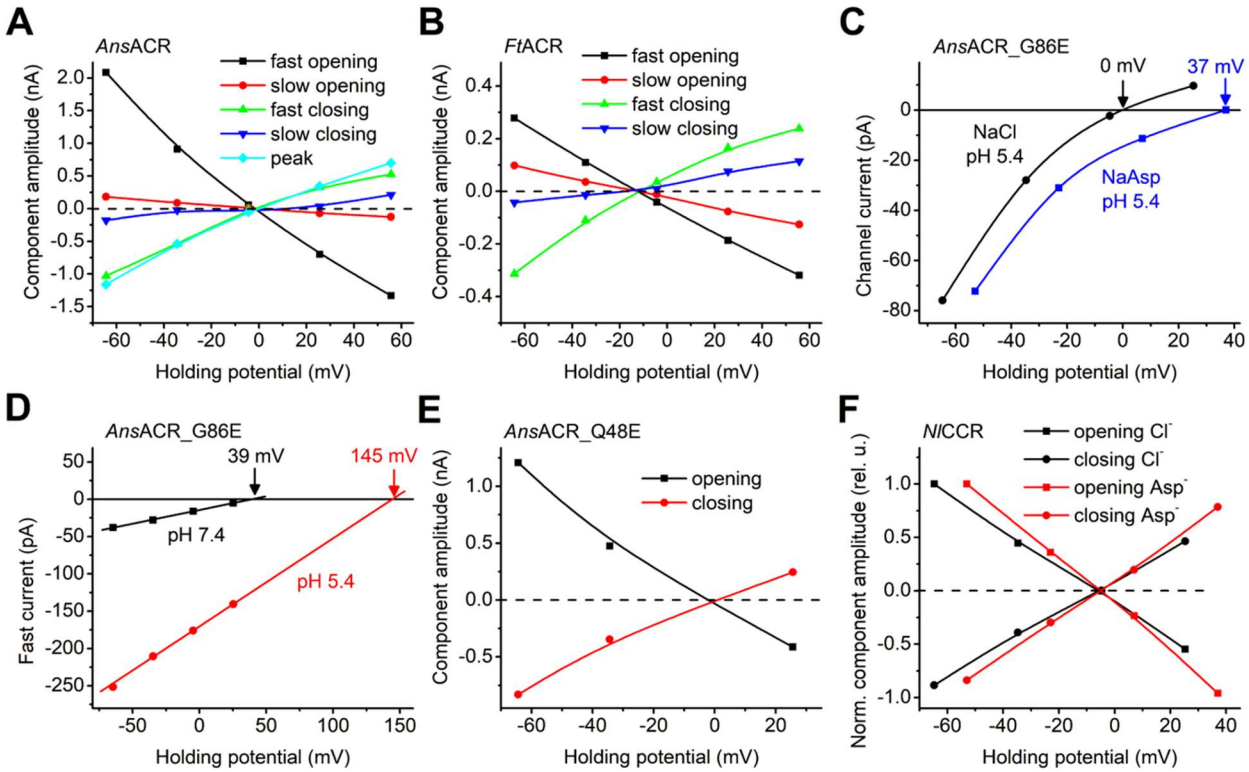

Figure 3 – figure supplement 1. Current-voltage relationships of photocurrent kinetic components. The amplitudes of the channel closing and opening components were estimated by multi-componential approximation of the laser-flash-evoked photocurrents.

The online version of this article includes the following source data for Figure 3 – figure supplement 1: Source data 1. Source data for the numerical values shown in (A-F).

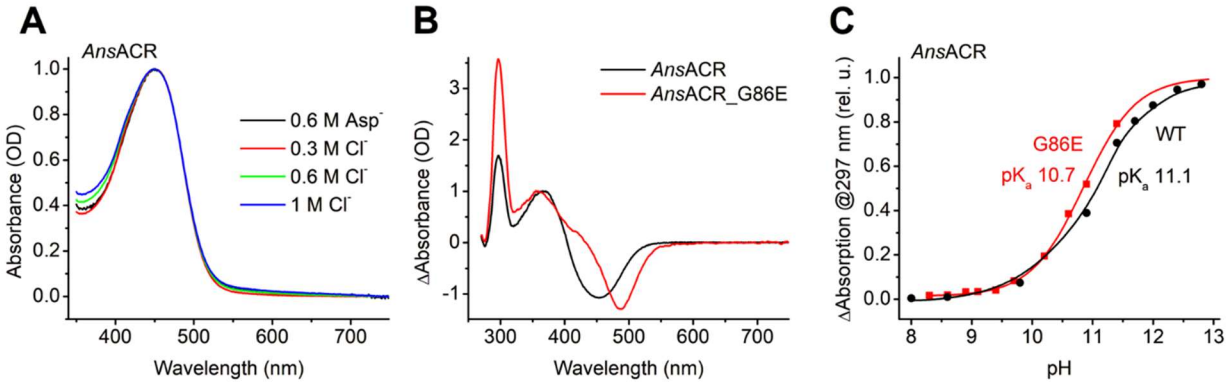

Figure 4 – figure supplement 1. Probing the RSB region in the wild-type *Ans*ACR and *Ans*ACR_G86E mutant.

(**A**) The absorption spectra of detergent-purified *Ans*ACR at the indicated Cl^- concentrations. (**B**) The difference spectra obtained upon alkalization. (**C**) pH titration of the absorbance difference at 297 nm.

The online version of this article includes the following source data for Figure 4 – figure supplement 1:
Source data 1. Source data for the numerical values shown in (C).

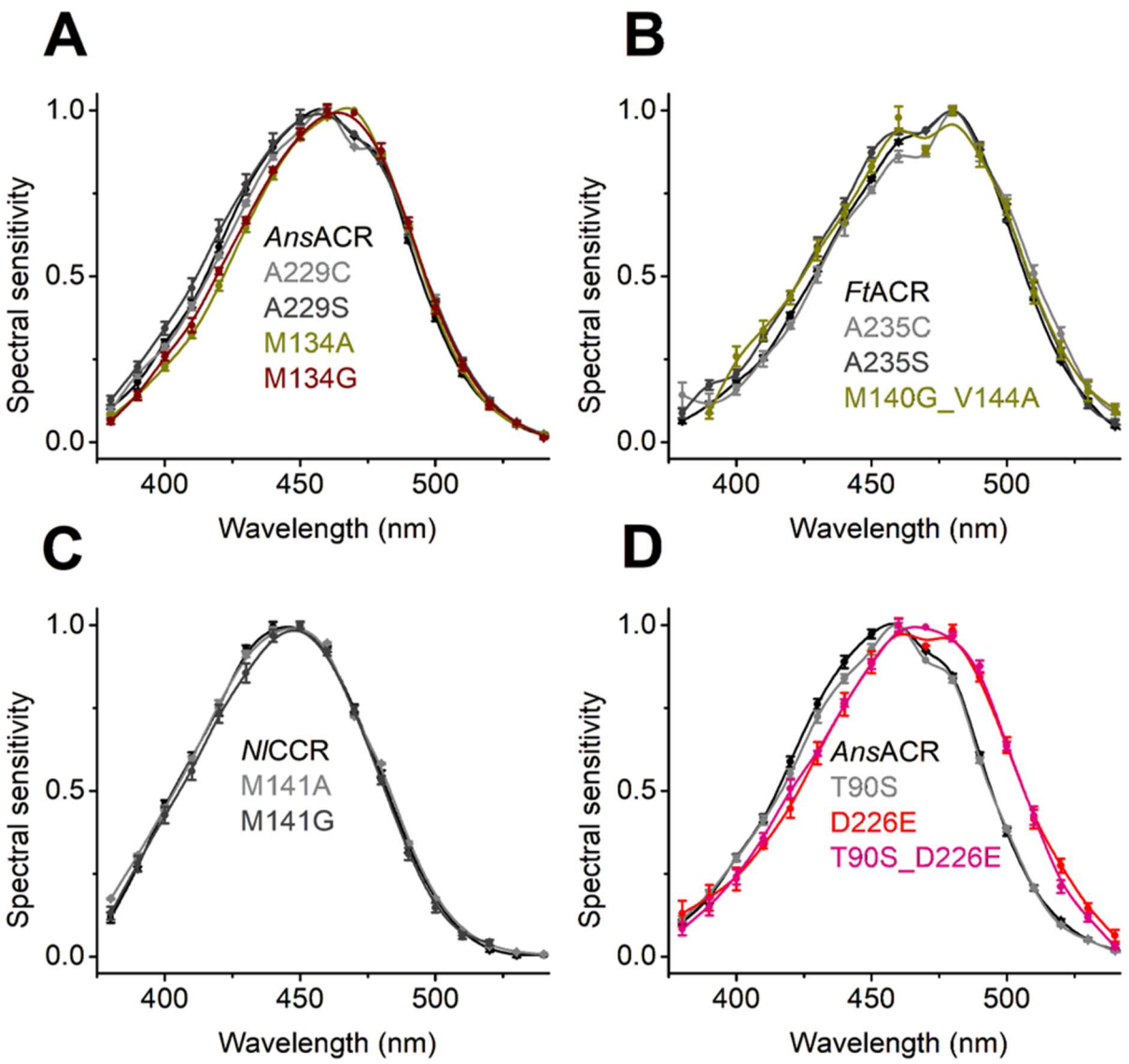

963 **Figure 5 – figure supplement 1. Mutations blue-shifting other microbial rhodopsins spectra do not affect**
964 **ancyromonad ChRs.**
965 The photocurrent action spectra of the indicated mutants compared to the respective WTs. The symbols
966 are the mean values, the error bars are SEM values.

967 The online version of this article includes the following source data for Figure 5 – figure supplement 1:
968 Source data 1. Source data for the numbers of cells sampled and numerical values shown in (A-D).

969

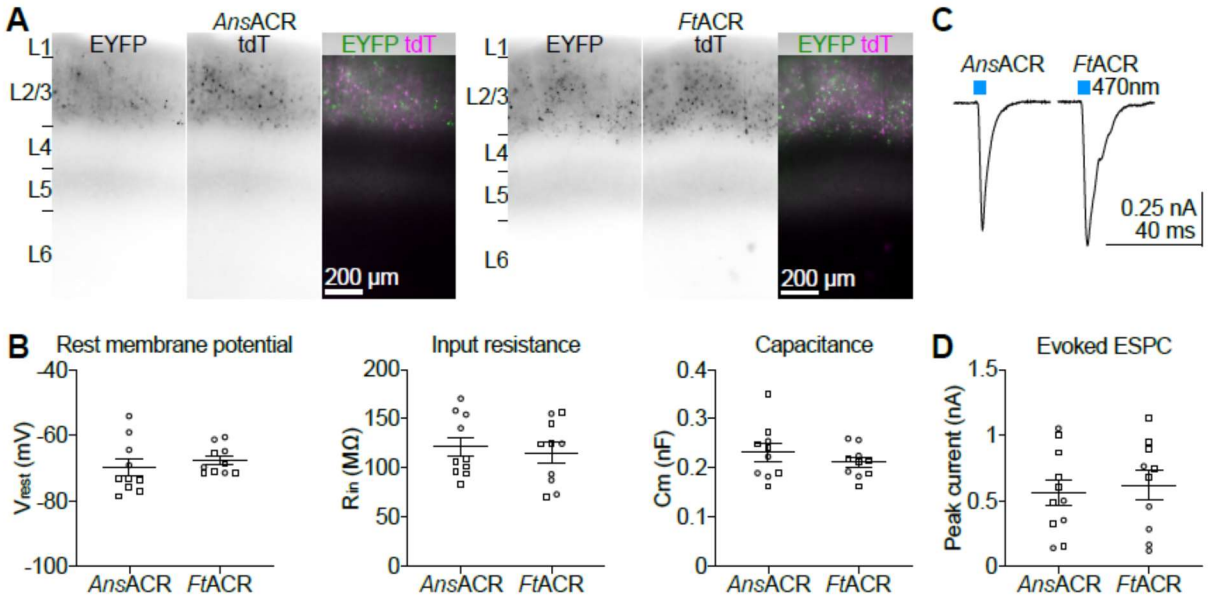

Figure 6 – figure supplement 1. Characterization of *Ans*ACR and *Ft*ACR expression in cortical neurons and axonal excitatory effect.

(**A**) Reprehensive fluorescence images of 300 µm-thick brain slices expressing tdTomato and EYFP fused to the C terminals of *Ans*ACR (left) and *Ft*ACR (right) in cortical layer 2/3 pyramidal neurons. The axons of ACR$^+$ layer 2/3 pyramidal neurons ramify in layer 5. L, layer. (**B**) Resting membrane potentials (left), input resistances (middle), and capacitances (right) of *Ans*ACR$^+$ and *Ft*ACR$^+$ neurons. (**C**) Representative traces of light-evoked excitatory post-synaptic currents (EPSCs) recorded from ACR$^-$ pyramidal neurons in layer 2/3 in response to 10-ms 470 nm light pulses (power density of 38.7 mW mm^{-2}). (**D**) Summary data of experiments in (C). The peak currents of light-evoked EPSCs were measured from the averaged current traces of three trials. In all panels, the data points from male mice are indicated by squares and female mice by circles. One male and one female mouse were used for each of the *Ans*ACR and *Ft*ACR experiments. Data are mean ± sem.

The online version of this article includes the following source data for Figure 6 – figure supplement 1:
Source data 1. Source data for the numbers of cells sampled and numerical values shown in (B, D).

985 **Supplementary Table 1. Compositions and liquid junction potential (LJP) values of the solutions used in**
986 **automated patch clamp recording.**

	KF	NaCl	KCl	Na aspartate	$NaNO_3$	NMDG Cl	$CaCl_2$	$MgCl_2$	HEPES	EGTA	glucose	LJP
Internal solution pH 7.2	110	10	10				2	1	10	10		
Standard external solution pH 7.4		140	4				2	1	10		5	7.3
Standard external solution pH 5.4		140	4				2	1	10		5	7.3
Na aspartate external solution			4	140			2	1	10		5	-4
$NaNO_3$ external solution			4		140		2	1	10		5	6.4
NMDG Cl external solution			4			140	2	1	10		5	13.5
KCl external solution			144				2	1	10		5	2.6

987